

Does mixed grain boundary follow the principles of superposition?

Author information

Wei Wan^{1,2} and Changxin Tang^{2,*}

¹ *Institute for Advanced Study, Nanchang University, Nanchang 330031, China*

² *Institute of Photovoltaics, Nanchang University, Nanchang 330031, China*

* *Corresponding author, Email address: tcx@ncu.edu.cn*

Abstract

One of the major challenges towards understanding and further utilizing the properties and functional behaviors of grain boundaries (GB) is the complexity of general GBs with mixed tilt and twist character. Here, we demonstrated that the structures and stress fields of mostly mixed GBs could be considered as the superposition of their tilt and twist GB components by computationally examining 26.8 million large-scale structures of 4964 unique silicon mixed GB characters. The results indicate that low angle mixed GB is formed by the dislocation interactions between its decomposed tilt and twist components, while various complex sub-structures with dislocation stress but without conventional dislocation core structures are discovered on twin and structural unit GBs. A universal Read-Shockley model that physically captures the energy trends of the mixed GB is proposed, and its superiority, universality and transferability are proven in a variety of GB structures across different lattices. The validity of this work is confirmed in the comparison with experimental observations and first-principles calculations. Earlier works should now be reassessed in the light of these findings.

Keywords: Grain boundary; Dislocation; Atomistic Simulation; Silicon

1. Introduction

What we know about grain boundaries (GBs) is that they are interfaces separating individual crystals with unique impacts on the structural and functional performances of crystalline materials, such as strength, plasticity, toughness, corrosion resistance and electronic activity [1–6]. Remarkable increments in these performances were made by controlling the population of desired GB types, which was an emerging field called grain boundary engineering (GBE) [7, 8]. Demands of GBE for silicon materials have been raised due to the rapid growth of the semiconductor and photovoltaic industries [9, 10]. Unfortunately, most of our knowledge about GBs was focused on FCC metals with low stacking fault energies [11–15]. To enable the GBE for silicon materials, the structure-property relationships of different GB types are required. In other words, we need to understand the basic GB structures and energetic properties that determine various GB behaviors (e.g., migration, diffusion, solute segregation and defect sink) [16–26].

Structures and properties of a given GB are jointly defined by the macroscopic and microscopic degrees of freedom (DOFs). The macroscopic DOFs are known as the five GB characters, three of them define the misorientation axis between two crystals and the other two describe the boundary plane normal. For each

unique macroscopic structural descriptor, numerous microscopic DOFs on the GB atomic arrangements have formed a multiplicity of meta-stable structures called GB phases, and their properties play a critical role in the material designs [27–29]. For accurately describing various GB structures at the atomic level, simulations are considered more insightful than experimental methods [30] because some of the complex GB structures are very difficult to experimentally access [31, 32]. Recent trends in this field are relying on the highly transferable artificial neural network interatomic potentials trained by first-principles datasets, which combine the advantages of both electronic structure methods (e.g., first-principles and tight-binding) and classical semi-empirical interatomic potentials and greatly balance their disadvantages [33–35]. Meanwhile, deep integrations between GB simulations and the growing machine-learning enable the characterization of almost all GB structures and their properties, which is known as the machine-learning representation of GB structure-property relationships [36–41].

Historically in the studies about GBs in silicon and other materials, the misorientation axis was often simplified down to the misorientation angle, which was based on simple geometry like symmetric tilt or twist [42–45]. Thus, one can define the simplest one-DOF GB on a specific boundary plane normal. The knowledge about the one-DOF GBs and their properties is extensive, including the Read-Shockley relationship [46] that predicts the GB structures and energies as a function of misorientation angle, the Frank-Bilby equation (FBE) [47, 48] for the predicting dislocation structures of low angle grain boundaries (LAGBs) [49–51], the structural and polyhedral unit models [52–54] characterizing GB structures at the atomic level, dislocation participation in shaping step-like GB disconnection structures [55, 56], the particularity (e.g., high occurrence of frequency, representativeness in the GB population) of low Σ (reciprocal density) Coincidence Site Lattice (CSL) GBs [12, 57], and the universality of GB structures among different FCC metals [58]. Beyond these findings, the topological analysis of the symmetry of 5D GB space yields a unique strategy named Fundamental Zone, which reveals the role of the boundary plane normal and the misorientation axis [59–62]. The latest computational approach [63] is capable of examining nearly the entire 5D GB space due to the rapid development of computer resources.

Although these reviewed studies almost constructed today's understandings of GB, they still lack comprehensive coverage of the possible GB characters because an arbitrary GB is not limited to the widely studied one-DOF symmetric tilt or twist types. Once geometrically favorable, the co-existence of symmetric tilt and twist DOFs occurs, which is known as the mixed tilt-twist GB character. Earlier works [64–66] have suggested that an analytical method for studying this GB type is through its decomposition into tilt and twist components with the nearest crystallographic distances, and addressing the correlations within. For example, LAGBs are often classified into tilt, twist and mixed types, where low angle symmetric tilt grain boundaries (LASTGBs) are often considered as dislocation arrays that fall in the prediction of FBE [67, 68], and low angle twist grain boundaries (LATwGBs) are suggested as dislocation networks with quadrate, hexagonal or more complex topology [69–73]. Going further, it has been experimentally and numerically shown that the low angle mixed grain boundaries (LAMGBs) contain dislocation characteristics of both of its components [66, 74–77]. Meanwhile, further knowledge about the mixed GB character and its structure-property relationships is quite limited [78], and therefore raised some intriguing questions: 1) What is their common

structural feature? 2) How does the property (e.g., energy and mobility) vary with the two DOFs? 3) Most importantly, can we transfer the knowledge about the one-DOF GBs to them?

In this atomistic study, we compute silicon mixed GB structures near the common $\langle 100 \rangle$, $\langle 110 \rangle$ and $\langle 111 \rangle$ misorientation axes with classical molecular mechanics. The unique protocol of this study is that the mixed GBs are studied by their decomposition into the tilt and twist components, which allows us to understand the correlations among tilt, twist and mixed tilt-twist GB geometry. Contrary to previous works that typically address GBs with only one DOF, we analyzed the mixed GBs within a 2D space and established a universal model on the basis of the classical Read-Shockley framework to characterize most of the mixed GB energies according to our findings.

2. Methodology

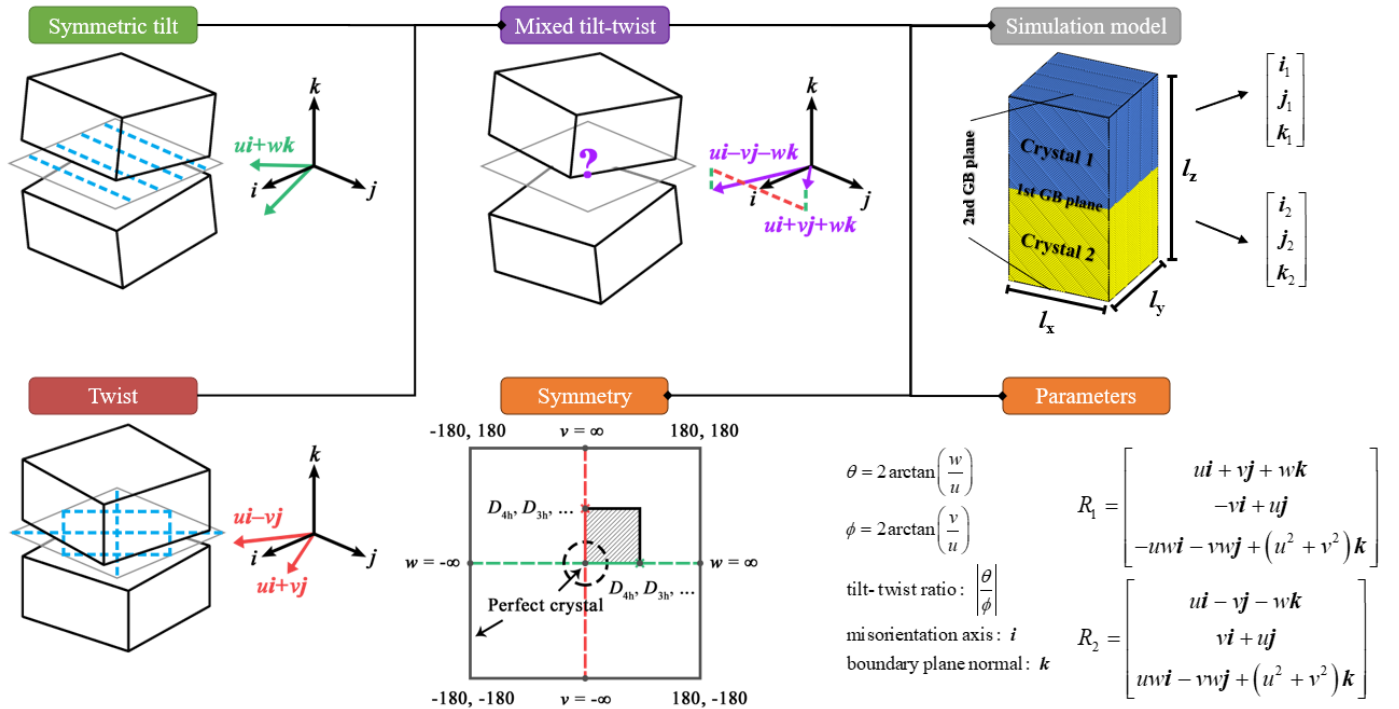


Figure 1. Geometry settings of the mixed tilt-twist GB character. A given mixed GB is generated in the ij plane with misorientation axis i and boundary plane normal k , and the rotation matrices of the upper crystal 1 and the lower crystal 2 are illustrated as $R_1 = [i_1, j_1, k_1]$ and $R_2 = [i_2, j_2, k_2]$. The mixed GB decomposes into a symmetric tilt grain boundary (STGB) with tilt angle θ and a twist grain boundary (TwGB) with twist angle ϕ at ik and ij planes, respectively. The co-existing tilt and twist angles create a 2D mixed character space, which symmetry is drawn in Figure 1. The domain of the mixed character space is $[-180^\circ, 180^\circ] \times [-180^\circ, 180^\circ]$. The domain center $(0^\circ, 0^\circ)$ and all four domain boundaries are perfect crystals or asymmetric tilt grain boundaries (ATGB, depending on the selection of i). LAMGB are found around the domain center (black dashed circle) and other positions where the perfect crystals appear (depending on the selection of i and k). The well-known STGBs and TwGBs are located in the 1D subsets $[-180^\circ, 180^\circ] \times [0^\circ]$ and $[0^\circ] \times [-180^\circ, 180^\circ]$, respectively. The symmetry of the axes i and k determines the perfect crystals and symmetric equivalence in the two mentioned 1D subsets (marked by the \times symbol; For example, 90° for D_{4h} symmetry and 180° for D_{2h} symmetry). Noting that the co-existing tilt and twist angles would make boundary plane normal k_1 and k_2 varies, and thus the indexing strategy using tilt and twist angles is unable to uniquely index a GB character. Strategies like Fundamental Zone [59] can give unique characterization.

The mixed GB are identified by their boundary plane and misorientation axis. For example, $(001)/[100]$ mixed GB denotes that the boundary plane is (001) while the misorientation axis is $[100]$. Three combinations of both boundary plane and misorientation axis are considered, including $(001)/[100]$, $(011)/[100]$ and

(111)/[110] mixed GBs. Each combination has a two-dimensional character space that is formed by the co-existing tilt and twist components. 1024 (32 STGBs and 32 TwGBs), 1536 (48 STGBs and 32 TwGBs) and 2304 (48 STGBs and 48 TwGBs) mixed GBs are sampled for (001)/[100], (011)/[100] and (111)/[110] mixed character spaces, respectively, which guarantee a comprehensive coverage at $\sim 3^\circ \times 3^\circ$ resolution. Tables S1-S6 (in the Supporting Information) show the details of sampled tilt and twist GBs, and Figure 1 shows the geometry of mixed GB.

LAMMPS [79] simulations are used to generate GB structures at zero temperature and pressure in a periodic box ($l_z \approx 2 \times \max(l_x, l_y)$ for LAGBs; $l_z = 20a$ for HAGBs) following the sampling method of Homer et al. [63]. In total, 26.8 million structures are examined for the 5344 GBs (4864 mixed, 256 symmetric tilt and 224 twist GBs). To the authors' knowledge, this number, as well as the GB size and structural richness that it represents have shown an order of magnitude greater than most of the reviewed minimum GB energy datasets [11, 14, 28, 30, 32–35, 43–45, 60].

Only classical interatomic potentials have the capability to minimize so many GB structures within acceptable costs. The authors adopted a modified Tersoff potential [80], which not only reproduces the elastic constants and generalized stacking fault energies of silicon but is also proven capable of modelling complex atomic bond environments and dislocation structures [66]. First-principles calculations and the involved methods [81–84] are used for parallel comparisons with atomistic simulations. The details are given in the Supporting Information.

The dislocation analysis tool (DXA) implemented in the software Ovito [85, 86] is used to identify dislocations structured LAGBs, setting the trial Burgers circuit length to 9 atom-to-atom steps and a default Burgers vector circuit stretchability.

GB energy E^{Total} from atomistic simulation and first-principles calculation are defined as the following:

$$E^{\text{Total}} = \frac{\sum_i^N (E_i - E_{\text{Coh}})}{A_{\text{GB}}} \quad (1)$$

Where N is the atom count of a GB in the simulation box (usually half of the box atoms because a box contains two GB). E_i is the energy of atom i , $E_{\text{Coh}} = -4.63\text{eV}$ is the cohesive energy of silicon atoms [87] and A_{GB} is the GB area size. The Virial stress tensor of each atom is also computed to show GB stress fields.

3. Results & Discussions

3.1. Grain Boundary Energy

3.1.1. Energy surface

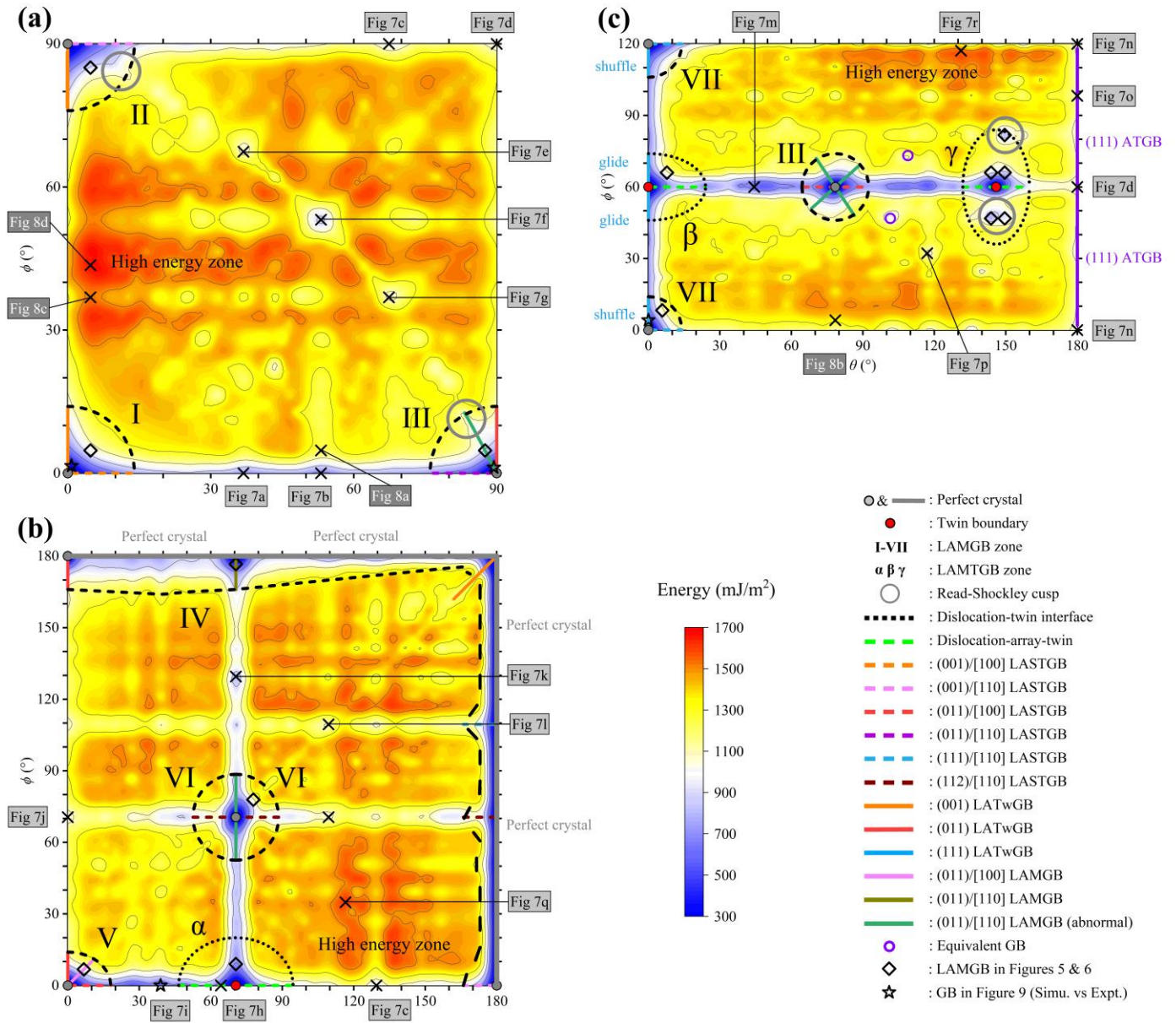


Figure 2. Energy surfaces of the examined mixed GBs as the functions of both tilt and twist angles. (a) (001)/[100] mixed GB; (b) (011)/[100] mixed GB; (c) (111)/[110] mixed GB.

Figures 2a, 2b and 2c show the (001)/[100], (011)/[100], (111)/[110] mixed GB energies as a continuous function of both tilt angle θ and twist angle ϕ , respectively. The three GB energy surfaces are plotted in the irreducible zone of the corresponding mixed character space, which size is constrained by the symmetry of the misorientation axes and boundary plane normal. Inspection of GB structures (dislocation analysis) indicates that all GB energy surfaces can be divided into two parts, low angle mixed grain boundaries (LAMGBs) comprised of dislocation structures (also include low angle mixed twin grain boundaries, called LAMTGBs, which are dislocation-twin structures) and high angle mixed grain boundaries (HAMGBs) comprised of amorphous structures, which are divided by the black dash line and named as the LAMGB zone,

LAMTGB zone, and HAMGB zone, respectively.

We first consider the seven unique LAMGB zones I to VII and the three unique LAMTGB zones α , β and γ in the three mixed character spaces. All mixed GB characters in the LAMGB zones are dislocation network structures where each dislocation segment is separated by perfect crystal. However, all mixed GB characters in the LAMTGB zones are dislocation network structures on the twin GB where each dislocation segment is separated by a twin structure. The ten unique LAMGB and LAMTGB zones are supposed to have elliptic shapes due to the symmetry of the energy surface shown in Figure 1, and thus some of the ten zones only show a quarter or a half. The vertices (in a quarter ellipse description/the center of the ellipse) of the ten zones are perfect crystal or twin GB, while some of the edges (in a quarter ellipse description) of the ten zones are low angle symmetric tilt grain boundaries (LASTGBs) or low angle twist grain boundaries (LATwGBs) or dislocation-array-twin (DAT) structures. It can be seen that these LASTGBs, LATwGBs and DAT structures represent the parts of the common 1D symmetric tilt or twist subsets that are frequently reported [11, 13, 14, 30, 32, 42–45, 69, 70]. Most importantly, the elliptic long and short axes that define the ten LAMGB and LAMTGB zones are determined by the core radius of dislocations in these LASTGBs, LATwGBs and DAT structures (i.e., dislocation core radius determines the curvature of each elliptic zone), where detailed explanation of such fact is referred to the authors' previous work. The dislocation structures of each zone will be shown in *Subsection 3.2.1*.

The energy trends of LAMGB zones I to VII are well captured by a revised Read-Shockley relationship that was established in the authors' earlier work, and the relationship will be further reinforced and extended in *Subsection 3.3.1* to capture the energy trends of LAMTGB zones α , β and γ , as well as the energy trends in the HAMGB zone. Even in the LAMGB zones where the dislocation density is proportional to the tilt and twist angles, one should notice that the energy trends are not completely smooth and show cusps, which are marked by the grey circles in Figure 2. These cusps actually reflect the physical facts of the LAMGB and LAMTGB zones as Read and Shockley [46] have already indicated that the cusps of LASTGBs (1D subset) appear when the dislocations are separated with equal distances. The situation becomes more complicated when comes to the 2D mixed character space, and a detailed explanation will be given later.

We then consider the three HAMGB zones in Figure 2. Generally speaking, there are various energy peaks which distribution forms a band-like landscape (marked as the high energy zone in Figure 2), along with numerous energy cusps that are distributed separately. The complexity of the three energy surfaces makes the modern GB energy functions that extrapolate from existing 1D subsets [88, 89] very difficult to predict the energy cusps therein. Beyond this, the energies of most HAMGBs are very close to the average energy of all examined GBs at around 1340 mJ/m^2 , which is a quite high value as the energies of mostly silicon HASTGBs are located at $\sim 800 \text{ mJ/m}^2$. One may also wish to predict the positions of energy cusps in the energy surface. By decomposing the mixed GBs into pure tilt and twist components, a rough correlation could be found between low energy HAMGB and low energy HASTGB/HATwGB. However, it is only a kind of preliminary observation while quantitative correlation is still difficult to extract.

More specifically, each energy surface has a unique geometry (regardless of the energy) that the perfect crystals, twin GBs and LAGBs are located in different positions, while the energy yields completely different

trends. For example, the HAMGB zone of (001)/[100] mixed GB in Figure 2a has more high energy HAMGB characters than the other two high angle zones. The perfect crystal is shown in three corner positions, accompanied by three LAMGB zones and the last corner position is a $\Sigma 3$ GB. This is because the bottom, up, left and right sides correspond to (001)/[100] STGB, (001)/[110] STGB, (001) TwGB, and (011) TwGB respectively.

The high angle zone of (011)/[100] mixed GB in Figure 2b is much more special than the former one as its bottom and left sides correspond to (011)/[100] STGB and (011) TwGB, respectively. All GB characters on its top and right sides are perfect crystals. This is because the tilt/twist misorientation is no longer functional when the twist/tilt angle is 180° ($v/u = \infty$ or $w/u = \infty$), as highlighted by Morawiec and Glowinski [64]. Two positions are perfect crystal and one position is twin GB if we exclude the top and right sides. Three notable deep trenches are located in the $\theta = 70.53^\circ$, $\phi = 70.53^\circ$ and $\phi = 109.47^\circ$ lines of this energy surface, separating the energy surface into smaller rectangles that are full of the peaks, and the lines correspond to (011)/[100] mixed GB, (112)/[110] and (111)/[110] STGBs, respectively.

For (111)/[110] mixed GB in Figure 2c, three positions showing perfect crystal and two positions showing twin GB. The bottom, top, left and right sides of Figure 2c correspond to (111)/[110] STGB, (111)/[110] STGB, (111) TwGB and (111) ATGB, respectively. The right side indexes ATGBs because the atomic layers along (111) are not crystallographic equivalent, though twist misorientation is not functional at $\theta = 180^\circ$. A deep trench representing (011)/[100] LASTGB is shown on the $\phi = 60^\circ$ line. Other mixed GBs around this line yield relatively low energy in the entire energy surface, suggesting a smooth transition to the high energy zone located near the top and bottom (i.e. the (111)/[110] STGB).

3.1.2. First-principles calculation

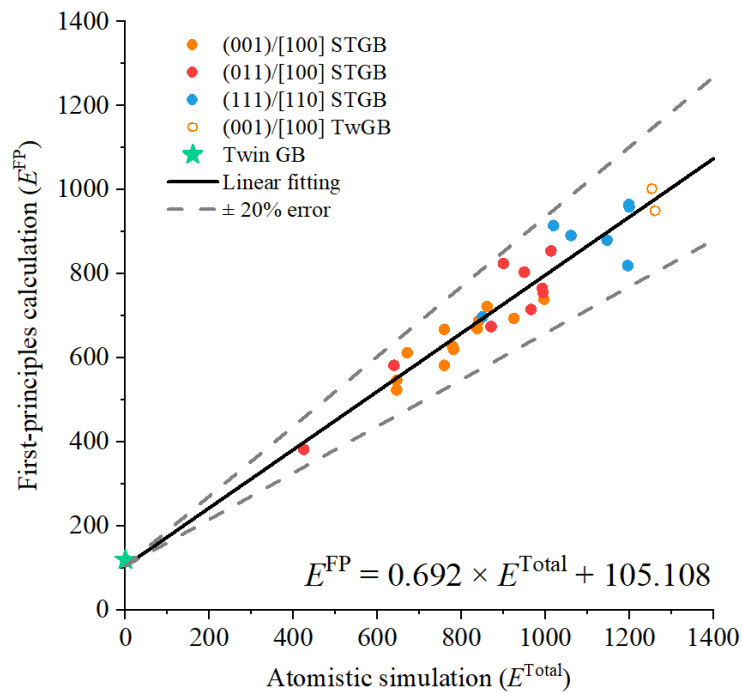


Figure 3. Comparison of calculated GB energies between atomistic simulation and first-principles calculation. Energy from atomistic simulation E^{Total} and energy from first-principles calculation E^{FP} follows the linear relationship $E^{FP} = 0.692 \times E^{Total} + 105.108$.

To validate the presented energy surface, GBs with low Σ values that fall in the acceptable computational range are submitted to the structural optimization of the first principles calculation. Unlike the atomistic simulation that reports nearly zero energy (0.04 mJ/m^2), the first principles calculation gives twin GB energy of 119.55 mJ/m^2 , both of which are very close to the published data of silicon and carbon [45]. The majority of the simulated energy is in good linear scaling with the first-principles calculation. All of the simulated energy falls in $\pm 20\%$ error lines, which suggests that the computed energy surface is reliable and can be extrapolated to first-principles results with the aid of the linear relationship in Figure 3. Also, this fact indicates that similar trends of the energy surface will be observed if more accurate (but consuming) computational methods are deployed, and the accuracy of semi-empirical interatomic potential is already capable of doing this.

3.2. Grain Boundary Structure

3.2.1. Dislocation structures

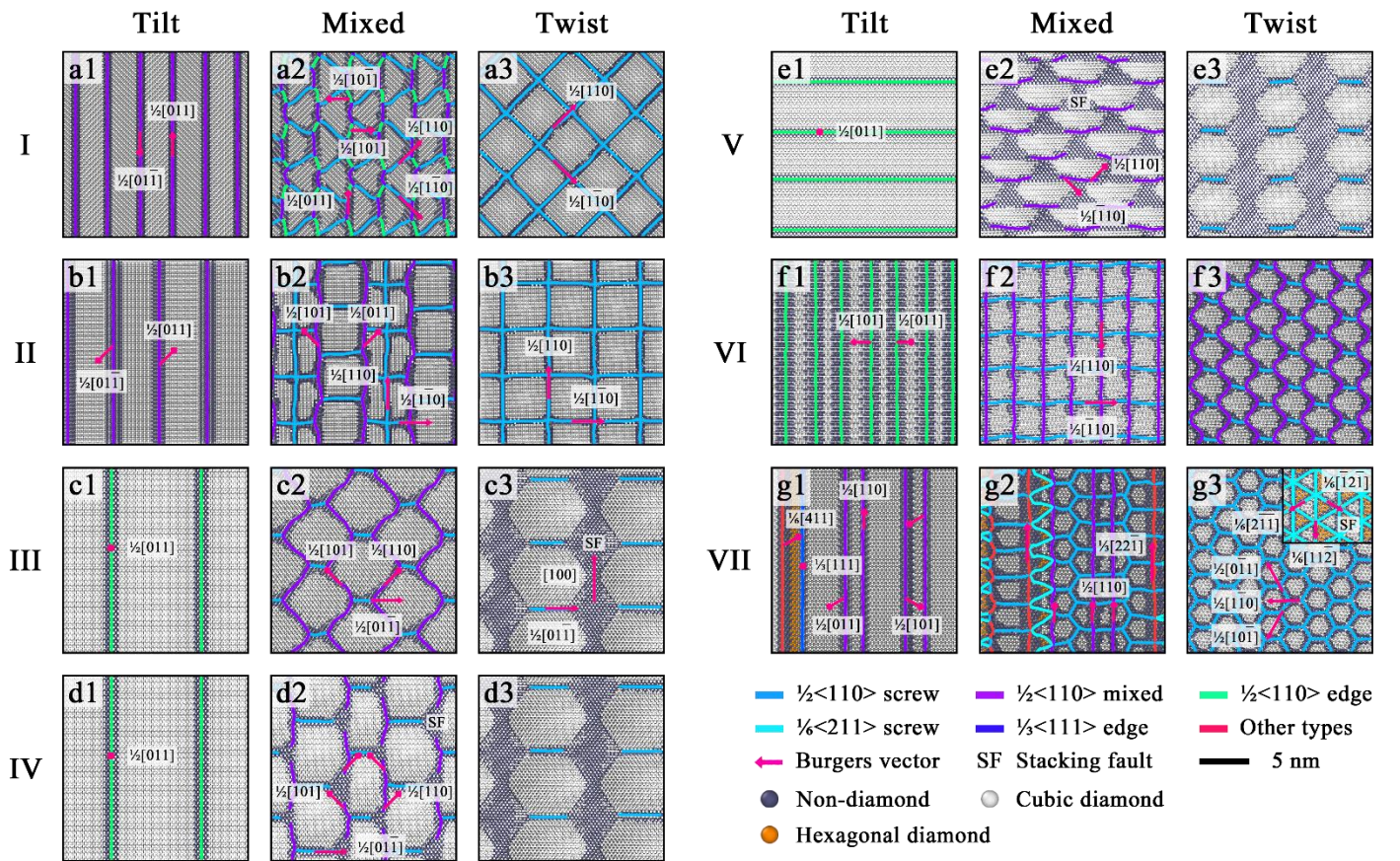


Figure 4. Dislocation structures of low angle symmetric tilt, twist and mixed GBs in the LAMGB zones I to VII of Figure 2. (a1) $\theta = 4.77^\circ$ (001)/[100] LASTGB; (a2) $\theta = 4.77^\circ$, $\phi = 4.77^\circ$ (001)/[100] LAMGB; (a3) $\phi = 4.77^\circ$ (001) LATwGB; (b1) $\theta = 3.38^\circ$ (001)/[110] LASTGB; (b2) $\theta = 3.38^\circ$, $\phi = 4.77^\circ$ (001)/[110] LAMGB; (b3) $\phi = 4.77^\circ$ (001) LATwGB; (c1) $\theta = 2.43^\circ$ (011)/[110] LASTGB; (c2) $\theta = 2.43^\circ$, $\phi = 3.39^\circ$ (011)/[110] abnormal LAMGB; (c3) $\phi = 3.39^\circ$ (011) LATwGB; (d1) $\theta = 2.43^\circ$ (011)/[110] LASTGB; (d2) $\theta = 2.43^\circ$, $\phi = 3.39^\circ$ (011)/[110] LAMGB; (d3) $\phi = 3.39^\circ$ (011) LATwGB; (e1) $\theta = 4.50^\circ$ (011)/[100] LASTGB; (e2) $\theta = 4.50^\circ$, $\phi = 4.50^\circ$ (011)/[100] LAMGB; (e3) $\phi = 4.50^\circ$ (011) LATwGB; (f1) $\theta = 7.91^\circ$ (112)/[110] LASTGB; (f2) $\theta = 7.91^\circ$, $\phi = 6.38^\circ$ (112)/[110] LAMGB; (f3) $\theta = 4.51^\circ$, $\phi = 6.38^\circ$ (011)/[110] abnormal LAMGB (mixed GB as the twist component); (g1) $\theta = 5.84^\circ$ (011)/[100] LASTGB; (g2) $\theta = 5.84^\circ$, $\phi = 8.26^\circ$ (011)/[100] LAMGB; (g3) $\phi = 8.26^\circ$ (011) shuffle LATwGB (the glide variant is in the small sub-figure);

The dislocation structures of seven LAMGBs in the LAMGB zones I to VII are shown in Figure 4, where all LASTGBs and LATwGBs are dislocation arrays and dislocation network (the (011) LATwGB is a hybrid dislocation and stacking fault network, also considered as dislocation network), respectively. Meanwhile, the topology of both the dislocation array and network would not change once the ratio between the tilt and twist angles (tilt-twist ratio, TTR) is determined. Such two facts depend on the inherent geometry definition of LAGBs (transferable among materials), which are acknowledged by these works [67, 68, 74]. In general, the seven LAMGBs (Figures 4a2 to 4g2) can be considered as the superposition of their tilt components (Figures 4a1 to 4g1) and twist components (Figures 4a3 to 4g3) after energetically favorable dislocation glide and reaction. The authors marked the types and Burgers vectors of each dislocation segment to make the dislocation glide and reaction easily traceable. In most LAMGBs, the dislocation glide and reaction mechanisms are based on $\frac{1}{2}\langle 110 \rangle$ screw dislocation, such as LAMGBs in Figures 4a2, 4b2, 4d2. The $\frac{1}{2}\langle 110 \rangle$ screw dislocation suffered segmentation from $\frac{1}{2}\langle 110 \rangle$ mixed dislocation, and then glide half of the screw dislocation spacing. There are more complex mechanisms involving the stacking faults from (011) LATwGB in Figures 4c2, 4d2 and 4e2. The two $\frac{1}{2}\langle 110 \rangle$ edge dislocations (i.e., (011)/[110] LASTGB and (011)/[100] LASTGB) separate both stacking fault (has a Burgers vector of $\langle 100 \rangle$) and $\frac{1}{2}\langle 110 \rangle$ screw dislocation of (011) LATwGB in two different orientations, which finally yields two different LAMGBs in Figures 4d2 and 4e2. Although the mechanisms governing (011) LAMGB structures are complicated and involve stacking fault, it indeed follows the same as the (001) LAMGB once we approximately consider the stacking fault as a dislocation. Even in the complex (111)/[110] LAMGB of Figure 4g2, the generation of the uncommon $\frac{1}{6}\langle 411 \rangle$ mixed and $\frac{1}{3}\langle 221 \rangle$ mixed dislocations are also caused by the dislocation reactions that including $\frac{1}{2}\langle 110 \rangle$ screw dislocation.

It should be noted that two LAMGB zones are been considered special or abnormal. The first zone is III, where all LAMGBs inside do not contain infinite, straight dislocation lines. The dislocation reaction is the same with the LAMGBs in zone IV, but the $\frac{1}{2}\langle 110 \rangle$ mixed dislocation glides to the edge of the stacking fault area and forms a zigzag pattern. LAMGB zone III decomposes exactly into the same tilt and twist components as zone IV. However, zone III cannot be indexed by examining the (011)/[110] energy surface in Figure 2, instead, it can be indexed by examining the (001)/[100] energy surface. The second zone is VI because its decomposed twist component is LAMGB in zone III rather than LATwGB. LAMGBs in zone VI is the superposition of (112)/[110] LASTGB and (011)/[110] LAMGB where the LAMGB plays the role of twist component.

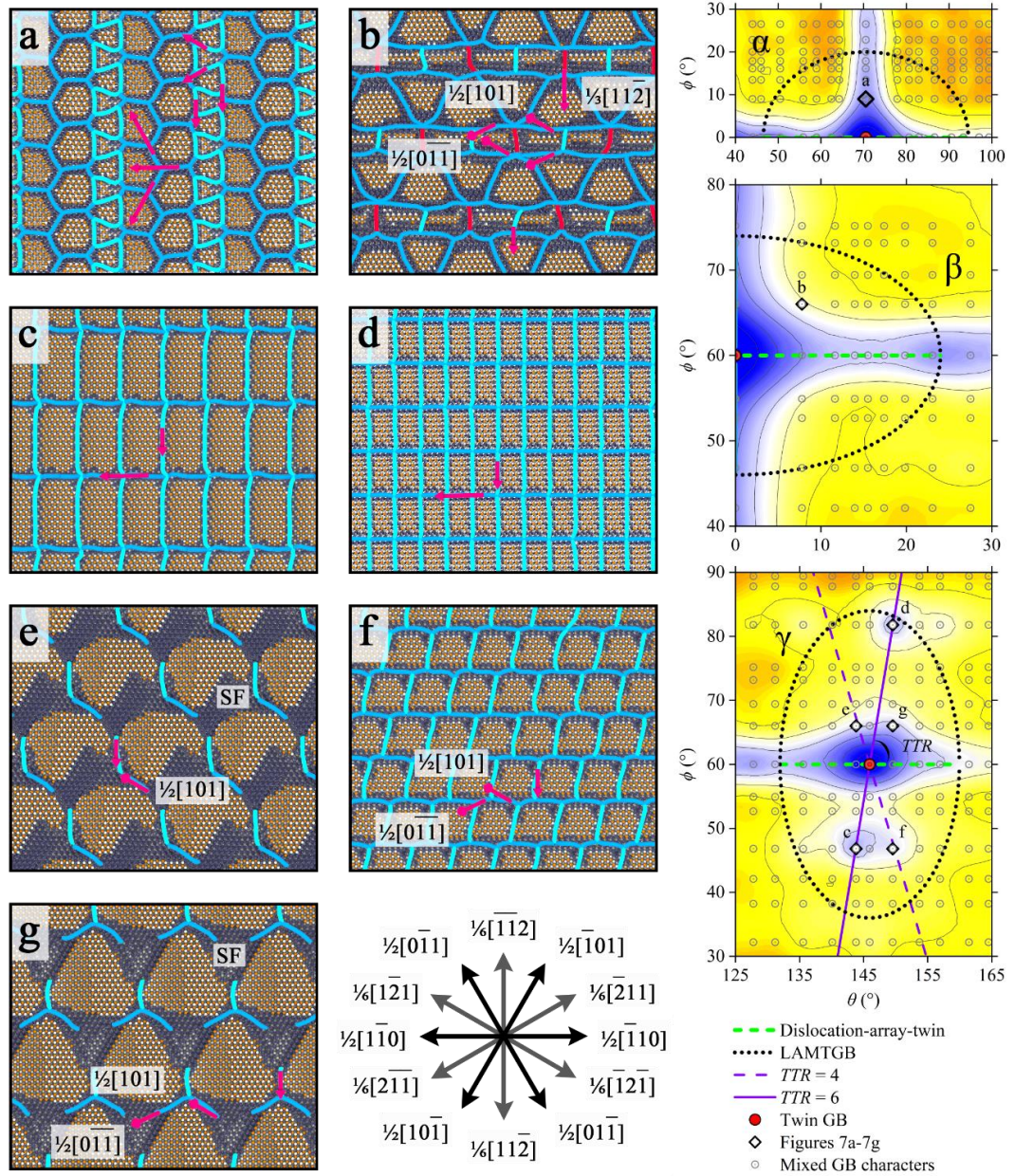


Figure 5. Dislocation structures of LAMTGBs (dislocation network on the twin GB) in the LAMTGB zones α , β and γ of Figure 2. Explanations of symbols follow the same in Figure 4.

Figure 5 shows the dislocation structures of seven LAMTGBs located in zones α , β and γ in Figure 2. The boundary plane normals of the seven LAMTGBs are found near the $\langle 111 \rangle$ and their misorientations are very close to the twin GB, which generates dislocation network structures on the twin GB. A major difference between the LAMTGB and LAMGB is that the LAMTGB is difficult to decompose into tilt and twist components. For example, the LAMTGB shown in Figure 5a cannot be decomposed into tilt and twist components. For example, if we assume that its tilt component is the twin GB while its twist component is the attached dislocation network, then it will contradict the fact that twin GB also plays as a twist component in Figure 2b. Beyond this fact that confuses the GB decomposition, the LAMTGBs in the three zones share a common feature with the LAMGB. It is that the topology of the dislocation network does not vary with the parameter TTR , which is proven by comparing LAMTGBs in Figures 5c and 5d that are located on the $TTR = 6$ lines in Figure 5. In summary, it can be seen that the twin GB could also accommodate complex dislocation structures, and the role of the twin GB is just like the perfect crystal in the mixed character space. This is

because the mixed GB characters near the twin GB are dislocation structures which topology depends on the parameter TTR . Although the formation mechanisms and the decomposition criterion of the LAMTGBs should be further explored, the authors are still optimistic about these results and conclusions as they show promising capability for interface engineering and self-assembled nanostructures.

3.2.2. Amorphous structures

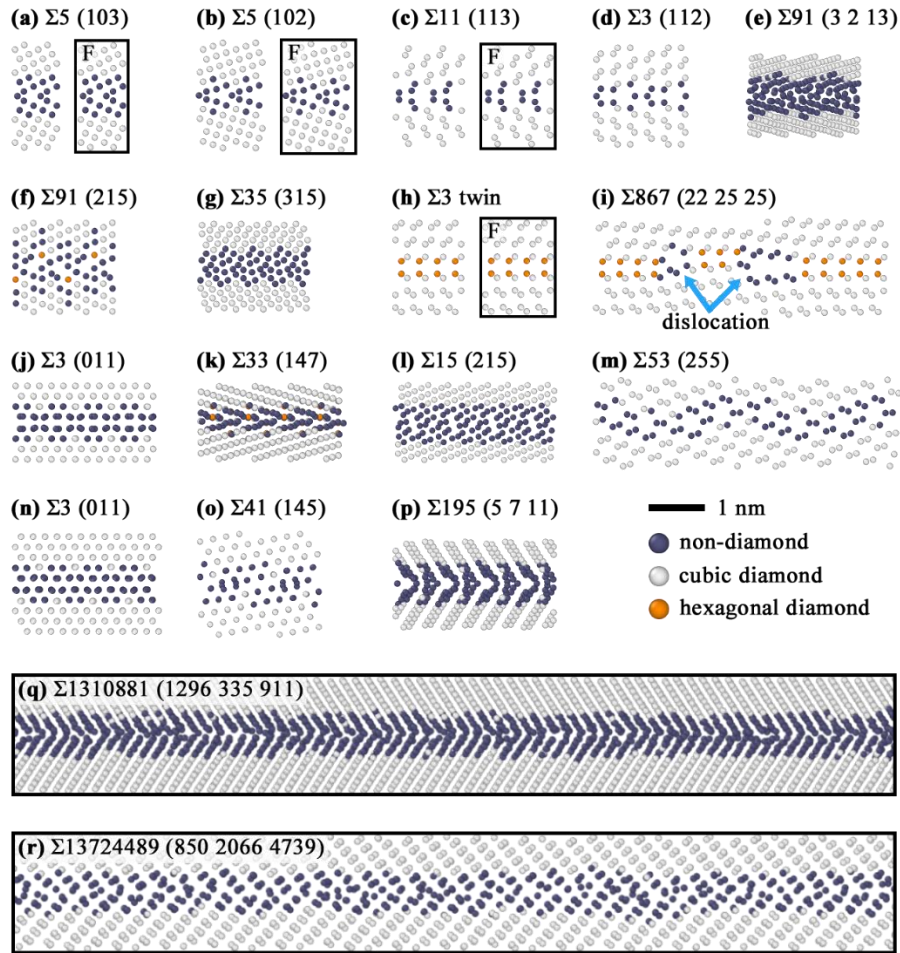


Figure 6. Atomic structures of various high angle symmetric tilt, twist and mixed GBs, where DXA reports no identifiable dislocation core structures. (a) to (r) correspond to GBs marked in Figure 2. Symbol F in the subfigures represents GB structures from First-principles calculations. Noting that only a part of the entire image is given for GBs in (q) and (r) due to the page limit

Figure 6 shows the atomic structures of HAGBs comprised of amorphous structures in Figure 2, where GBs in Figures 6a-6d and 6m show typical symmetric tilt characteristics near the $[100]$ and $[110]$ axes. First-principles calculation reports good agreement with atomistic simulation on the structures of these simple HASTGB. GBs in Figures 6e, 6k, 6l and 6p are HAMGB comprised of large and complex structural units, and these HAMGB appear in transition between structural units and completely amorphous structures. The two GBs in Figures 6f and 6g are extracted from the $(001)/[100]$ mixed GB population. They should be considered as HASTGB due to the coincident sites of the adjacent crystals, although they are indexed in the HAMGB zone in the $(001)/[100]$ energy surface in Figure 2a. The reason causes such an indexing problem is that the tilt angle and twist angle are defined on their misorientation axes separately, and the mixed GBs inside the mixed character space sustain the angular deviation of both. Figures 6h and 6i are twin GB and dislocation-array-twin GB. The dislocation-array-twin GB is formed by introducing a small tilt angle around the tilt axis

[110] on the twin GB. Note that the atoms forming the twin interface are identified as the hexagonal diamond type in Ovito. Figures 6j and 6n are two (011) HATwGBs, and Figure 6o gives the atomic structures of a [111] ATGB, where an angular deviation between the boundary plane and symmetry plane is introduced to form an asymmetric tilt angle. Figures 6q and 6r show HAMGBs with the highest energy in (011)/[100] and (111)/[110] energy surfaces, respectively. These high energy HAMGBs usually have very large DSC cell sizes and very high Σ values so the structural unit model is no longer applicable (i.e., the structural unit is too big). Noting that these GBs are completely amorphous structures with extremely high energy at around 1600 mJ/m², and most importantly, the lattice distortion (proportional to energy) they represented seems to reach a maximum limit that a GB can tolerate. It appears that these GBs fall into the prediction of a very early model (inter-crystalline amorphous cement theory) that describes GB as a thin layer of supercooled liquid [90].

Generally speaking, most of the results given in Figure 6 are unsurprising, but they are still presented with DFT calculation results together to validate the capability of atomistic simulation for capturing those simple GB structures. Figure 6 also illustrates the unique structural richness of the mixed GBs dataset sampled here, and the massive information it contains at the micro-structure level still needs to be further extracted in machine-learning approaches on GB structure-property relationships.

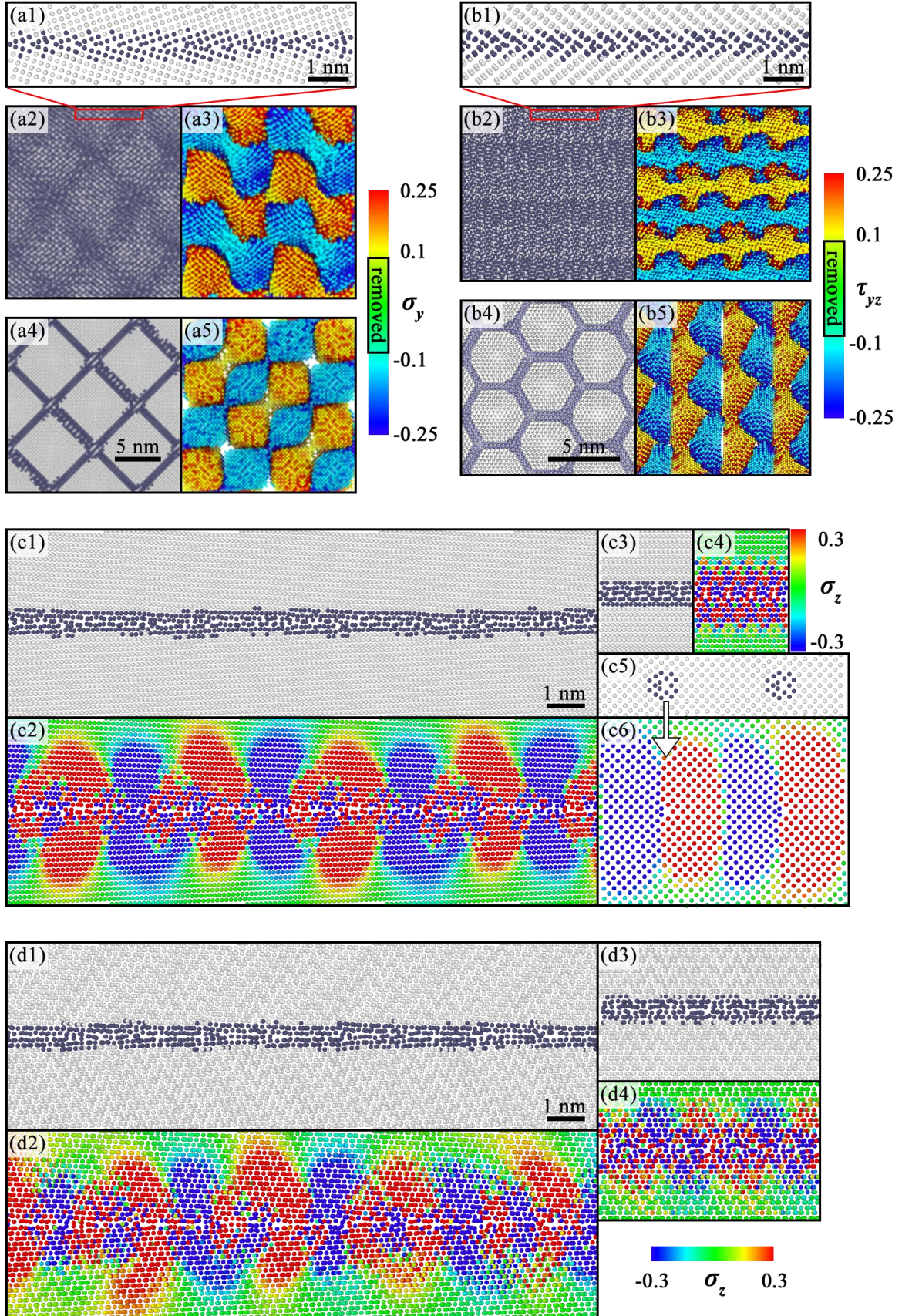


Figure 7. Atomic structures and stress fields of HAMGBs in Figure 2. (a1) Side view of atomic structures of a $\Sigma 26001$ (288 12 577) HAMGB, which is formed by introducing a 4.77° twist angle on the $\theta = 53.13^\circ \Sigma 5$ (102) STGB; (a2) Upper view of atomic structures of the $\Sigma 26001$ (288 12 577) HAMGB; (a3) Upper view of distribution of stress component σ_y of the $\Sigma 26001$ (288 12 577) HAMGB; (a4) Upper view of atomic structures of the $\phi = 4.77^\circ$ (001) LATwGB (the same with Figure 4a3); (a5) Upper view of distribution of stress component σ_y of the (001) LATwGB; (b1) Side view of atomic structures of a $\Sigma 328363$ (507 5 267) HAMGB, which is formed by introducing a 4.13° twist angle on the $\theta = 78.46^\circ \Sigma 15$ (201) STGB; (b2) Upper

view of atomic structures of the $\Sigma 328363$ (507 5 267) HAMGB; (b3) Upper view of distribution of stress component τ_{yz} of the $\Sigma 328363$ (507 5 267) HAMGB; (b4) Upper view of atomic structures of the $\phi = 4.13^\circ$ (111) LATwGB; (b5) Upper view of distribution of stress component τ_{yz} of the (111) LATwGB; (c1) Side view of atomic structures of a $\Sigma 3605$ (2 1 60) HAMGB, which is formed by introducing a 4.77° tilt angle on the $\phi = 36.87^\circ$ $\Sigma 5$ (001) TwGB; (c2) Side view of distribution of stress component of the $\Sigma 3605$ (2 1 60) HAMGB; (c3) Side view of atomic structures of a $\phi = 53.13^\circ$ $\Sigma 5$ (012) TwGB; (c4) Side view of distribution of stress component of the $\phi = 53.13^\circ$ $\Sigma 5$ (012) TwGB; (c5) Side view of atomic structures of a $\theta = 4.77^\circ$ (001)/[100] LASTGB; (c6) Side view of distribution of stress component σ_z of the $\theta = 4.77^\circ$ (001)/[100] LASTGB; (d1) Side view of atomic structures of a $\Sigma 485141$ (25 10 696) HAMGB, which is formed by introducing a 4.77° tilt angle on the $\phi = 43.60^\circ$ $\Sigma 29$ (025) TwGB; (d2) Side view of distribution of stress component σ_z of the $\Sigma 485141$ (25 10 696) HAMGB; (d3) Side view of atomic structures of a $\phi = 43.60^\circ$ $\Sigma 29$ (025) TwGB; (d4) Side view of distribution of stress component of the $\phi = 43.60^\circ$ $\Sigma 29$ (025) TwGB.

Figure 7 shows the atomic structures of four HAMGBs without dislocation core structures but with typical dislocation stress fields. Figure 7a1 is the atomic structures of a near $\Sigma 5$ HAMGB that is created by introducing a low twist angle ($\phi = 4.77^\circ$) on the boundary plane normal ($\langle 001 \rangle$) of the well-known kite-shaped $\Sigma 5$ STGB shown in Figure 6a. The view along its boundary plane normal in Figure 7a2 indicates a squared shadow pattern, which follows the same spacing compared with the squared screw dislocation network of a $\phi = 4.77^\circ$ (001) LATwGB. The stress fields of the HAMGB in Figure 7a3 are also similar to the dislocation stress fields of the LATwGB in Figure 7a5. Figure 7b1 is the atomic structures of a near $\Sigma 15$ HAMGB created by introducing a low twist angle ($\phi = 4.13^\circ$) on the boundary plane normal ($\langle 111 \rangle$) of a $\Sigma 15$ STGB. The HAMGB also generates different but considerable stress fields as compared with its twist component, a $\phi = 4.13^\circ$ (111) LATwGB. The authors regard that differences between the shapes of stress fields in Figure 7b3 (HAMGB) and 7b5 (HAMGB twist component) come from the superposition and mutual perturbation of the stress fields from the $\Sigma 15$ STGB and the $\phi = 4.13^\circ$ (111) LATwGB. To verify such an explanation, the other two HAMGBs and their stress fields are given in Figures 7c1 and 7d1, where their tilt components are the $\theta = 4.77^\circ$ (001)/[100] LASTGB shown in Figure 7c5. We can see that the stress fields of the two HAMGBs show the same stress characteristics compared with the dislocation stress fields in Figure 7c6, although both of them are completely amorphous structures without any identifiable dislocation core or structural units. However, the dislocation stress fields shown in Figure 7c2 are more remarkable than the counterparts shown in Figure 7c3, which is explained by the complexity of their twist components. For instance, the structural units of the (001) TwGBs corresponding to the two HAMGBs c1 and d1 are given in Figures 7c3 and 7d3. Obviously, the structural unit in Figure 7c3 has a lower repeated cell size than the one in Figure 7d3, which simplifies its stress characteristics and finally results in more remarkable dislocation stress fields.

By addressing correlations of stress fields between HAMGBs and their components, and comparing the situations that a STGB accommodating a low twist angle and a TwGB accommodates a low tilt angle, it is found that the stress fields of any mixed GB with a low angle component are the superposition of its tilt and twist component's stress fields. Such superposition also depends on the structural complexity of the tilt/twist GB that accommodates the low angle twist/tilt component as GBs comprised of simple structural units have higher capability to maintain the dislocation stress fields. Most importantly, these findings suggest that the energies of these amorphous GB structures do not completely come from lattice disorder. In fact, the elastic

strain energy plays a critical role in the structure-energy relationships of these HAMGBs, which could be further described in the framework of the classical Read-Shockley relationship.

3.2.3. Comparison with experiments

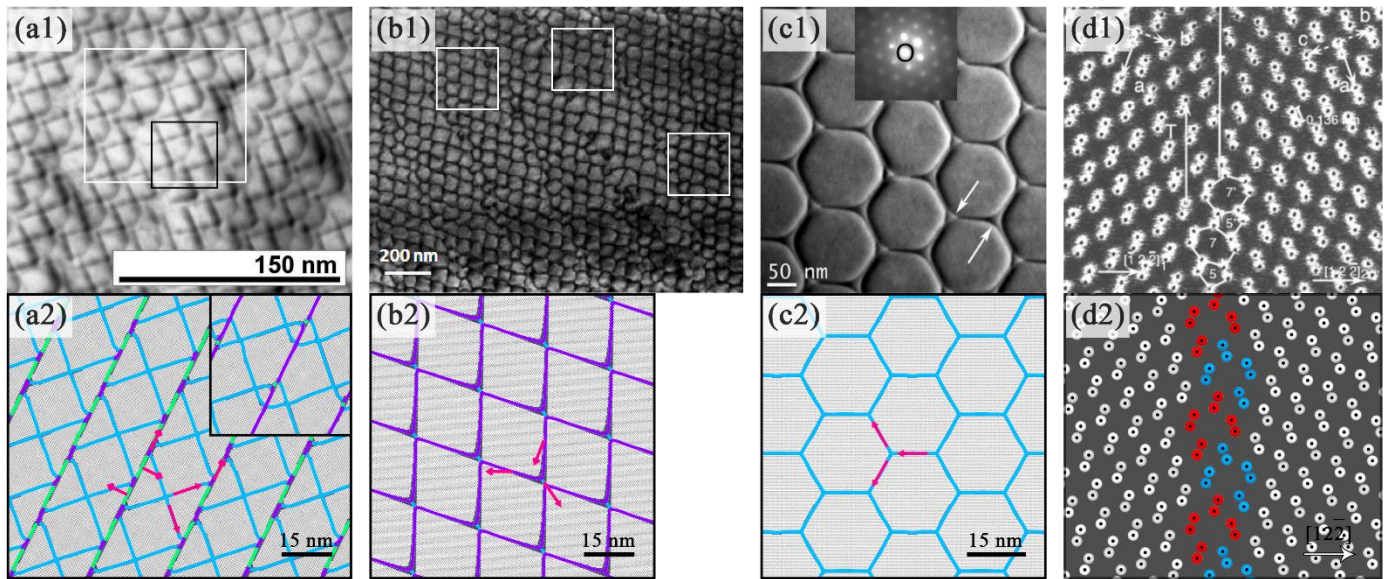


Figure 8. Comparisons between experimental observations and atomistic simulations. (a1) Experimental observation of a (001) LAMGB from Wilhelm et al. [77]; (a2) 1:1 atomistic simulation reproduction of the (001) LAMGB structures at the stable state, the subfigure indicates a meta-stable state of the (001) LAMGB structures; (b1) Experimental observation of a (011) LAMGB from Reiche et al. [91]; (b2) 1:2.66 atomistic simulation reproduction of the (011) LAMGB structures at the stable state. The comparison mainly focuses on the dislocation network topology as the dislocation spacing is proportional to both θ and ϕ ; (c1) Experimental observation of a (111) LATwGB from Neily et al. [72]. The hexagonal dislocation network shows partial dissociation to triangular hybrid dislocation and stacking fault at the dislocation triple junctions; (c2) 1:7 atomistic simulation reproduction of the (111) LATwGB structures at the stable state. The stable (111) LATwGB has hexagonal dislocation network structures that correspond to the (111) shuffle plane, while the triangular hybrid dislocation and stacking fault structures of the (111) glide plane are metastable; (d1) Experimental observation of a (011) HASTGB from Bonnet, et al. [92]; (d2) 1:1 atomistic simulation reproduction of the (011) HASTGB structures at the stable state. The error of each atom position is less than 0.01 nm.

Figure 8 shows the comparisons between experimental observations and atomistic simulations of four silicon GBs, where Figures 8a1 and 8a2 show a (001) LAMGB, Figures 8b1 and 8b2 show two (011) LAMGBs with the same parameter TTR , Figures 8c1 and 8c2 show two (111) LATwGBs with the same parameter TTR , and Figures 8d1 and 8d2 show a (011) HASTGB. The positions (in the mixed character space) of the simulated GBs 8a2, 8b2, 8c2 and 8d2 used in comparison have been marked in Figure 2. It is surprising that the simulation shows the unique capability to accurately reproduce both dislocation and amorphous silicon GB structures at the atomic level. For example, the experiments versus simulation is 1:1 in the length scale for GBs in Figures 8a and 8d. The simulation reproduces the complex topology of the dislocation network across the nano-scale, and even the meta-stable dislocation network structures partially shown in Figure 8a1 are captured, which is given in the subfigure of Figure 8a2. Such success demonstrates that the simulated dislocation structures in Figure 4 are reliable. Meanwhile, for the dislocation structures shown in Figures 8b1 and Figure 8c1, the validity is further addressed in comparisons between the dislocation network topology. The experimentally observed dislocation network structures are not required to be reproduced with the 1:1

ratio as this would make the computational resources unbearable. The authors are focused on the topology and its related parameter TTR using the useful conclusion that the dislocation network topology only depends on TTR . The conclusion allows the simulation to reproduce the dislocation network structures of LAMGBs in a designated scale like 1:2.66 or 1:7. The simulation shows well accordance with the experimentally observed (011) LAMGB and the (111) LATwGB, but the atomistic simulation at zero temperature and pressure fails to capture the dislocation dissociation at the triple junctions of (111) LATwGB at the finite temperatures. It is actually acceptable as the simulation predicts the (111) shuffle LATwGB (hexagonal $\frac{1}{2}\langle 110 \rangle$ dislocation network) is the stable state rather than the (111) glide LATwGB (triangular hybrid $\frac{1}{6}\langle 211 \rangle$ dislocation and stacking fault network) with slightly higher energy. The finite temperature experiment in Figure 8c1 has shown their mutual conversion. More detailed understandings of the difference and mutual conversion between (111) shuffle and glide planes in silicon and FCC metals are referred to in these works [45, 93, 94]. For the structural unit GB shown in Figure 8d1, the simulation presents an unexpected excellent agreement, the error of each atom position is sub-angstrom level. The simulation results in Figure 8d2 indicate that our simulation method and the selected interatomic potential not only reproduce the dislocation structures of LAGBs but also capture the atomic bond environment in HAGBs that are often considered as amorphous structures. In summary, the comparison between experiments and simulations proves the fact that most of the simulated structures given here are reliable, and further verifies the conclusion that the LAMGBs are indeed the superposition of their tilt and twist components.

3.3. A universal Read-Shockley model

3.3.1. Theorization

On the basis of the results and discussions presented in *Subsections 3.1 to 3.3*, the authors are able to present a general framework that is universal for the structures and energies of mostly GBs spanning the mixed character space. First of all, we summarized a qualitative estimation strategy of the structures, energies and stress fields of a given mixed GB from its decomposed components in Figure 9, which would be useful in the preliminary analysis.

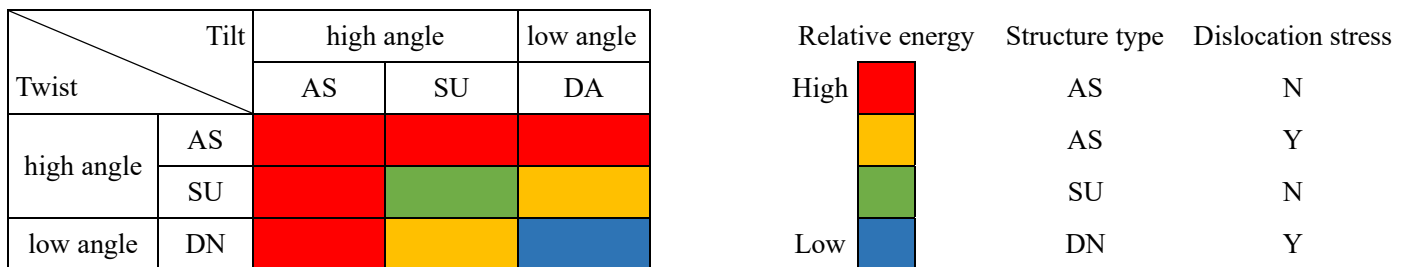


Figure 9. Qualitative estimation strategy of mixed GB structures, energies and stress fields through the tilt and twist components. AS: amorphous structures (no identifiable structural units or structural unit size is very large); SU: (structural unit); DA: dislocation array; DN: dislocation network. AS mixed with any structures will result in a relatively high energy, and SU mixed with SU usually yields a SU. All LAMGBs (DA mixed with DN) are DN with the relatively lowest energy.

Then, we considered quantifying the mixed GB energy. For each LAMGB zone in Figure 2, the LAMGB energy can be divided into dislocation core energy and dislocation strain energy. The dislocation network structures of the LAMGBs there are the superpositions of their tilt and twist components after subjecting to

energetically favorable dislocation glide and reaction. The geometry descriptions of the LAMGBs, like the Burgers vector and dislocation density, strictly follow the conservation law, which also means that the dislocation core energy of each LAMGB is equal to the sum of the dislocation core energy of the LAMGB tilt components and LAMGB twist components minus the loss of dislocation core energy when the tilt and twist components join together to form the LAMGB. As for the dislocation strain energy of the LAMGB, there are multiple groups of periodic dislocation segments from the tilt and twist components that exist simultaneously in the LAMGB, which causes a mutual perturbation between the original stress fields of both independent tilt and twist components. In that way, the LAMGB energy E could be written as the function of both tilt angle θ and twist angle ϕ following

$$E_{\text{LAMGB}}^{\text{Total}}(\theta, \phi) = E_{\text{LASTGB}}^{\text{Total}}(\theta) + E_{\text{LATwGB}}^{\text{Total}}(\phi) + E_{\text{Loss}}^{\text{Core}} + E_{\text{Loss}}^{\text{Strain}} \quad (2)$$

Where superscript Total, Core and Strain denote the total excess energy of a LAMGB, the dislocation core energy and the dislocation strain energy, respectively. Subscript LAMGB, LASTGB and LATwGB denote the corresponding GB type. Subscript Loss denotes the energy loss from the energetically favorable dislocation glide and reaction process. Equation (2) is purely the preliminary analytical expression of the LAMGB energy as a function of tilt and twist angles, and Read and Shockley have already given the analytical expression of the LASTGB and LATwGB energies known as the classical Read-Shockley relationship ($\theta - \theta \ln(\theta)$ and $\phi - \phi \ln(\phi)$) for the first two terms of equation (2), but note that the detailed expressions within the last two terms are still unclear. An empirical expression of the last two terms of equation (2) that takes the Read-Shockley formalism has been proposed by the authors in their earlier work [66], which is called the revised Read-Shockley relationship. It is given as the following:

$$E_{\text{LAMGB}}^{\text{Total}}(\theta, \phi) = \theta \left[E_{\text{LASTGB}}^{\text{Core}} - E_{\text{LASTGB}}^{\text{Strain}} \ln(\theta) \right] + \phi \left[E_{\text{LATwGB}}^{\text{Core}} - E_{\text{LATwGB}}^{\text{Strain}} \ln(\phi) \right] + \theta \phi \left[E_{\text{Loss}}^{\text{Core}} - E_{\text{Loss}}^{\text{Strain}} \ln(\theta \phi) \right] \quad (3)$$

Where the last two terms $E_{\text{Loss}}^{\text{Core}} + E_{\text{Loss}}^{\text{Strain}}$ that take the Read-Shockley formalism $\theta \phi - \theta \phi \ln(\theta \phi)$ are considered to have a good balance of both fitting effects and clarity [66]. Sutton and Balluffi have highlighted that the correlations between misorientation angles and energies of any LAMGB energy should follow or be similar to the Read-Shockley formalism, while the empirical expression presented in equation (3) automatically satisfies such requirements, and its potentiality (prediction of the GB energy trends, compatibility and applicability) will be further demonstrated and reinforced here soon.

We first show the great compatibility of equation (3). For example, by replacing θ and ϕ with $\sin(\theta)$ and $\sin(\phi)$, Equation (3) becomes the Wolf's version of the Read-Shockley relationship [95]. Equation (3) can accommodate an additional energy term E_i to describe the interaction between different dislocation segments in the dislocation network of LATwGB, as Vitek did [96]. As for the LAMTGB shown in Figure 4, they follow the same dislocation glide and reaction mechanisms as the authors previously described for the LAMGB. Since the LAMTGBs are dislocation structures on the twin GB, an additional term E_{twin} that denotes the twin GB energy must be appended to equation (3) to capture the energy trends in the LAMTGB zone following:

$$E_{\text{LAMTGB}}^{\text{Total}}(\theta, \phi) = \theta \left[E_{\text{LASTGB}}^{\text{Core}} - E_{\text{LASTGB}}^{\text{Strain}} \ln(\theta) \right] + \phi \left[E_{\text{LATwGB}}^{\text{Core}} - E_{\text{LATwGB}}^{\text{Strain}} \ln(\phi) \right] + \theta \phi \left[E_{\text{Loss}}^{\text{Core}} - E_{\text{Loss}}^{\text{Strain}} \ln(\theta \phi) \right] + E_{\text{Twin}} \quad (4)$$

Equation (4) is supposed to be applicable after identifying the tilt and twist components of LAMTGBs.

Most importantly, equation (3) and its variant are not only applicable for dislocation structured and dislocation-twin structured GBs but also applicable for some of the mixed GBs comprised of completely amorphous structures. For example, the mixed GB structures shown in Figure 4 are completely amorphous structures without any ordered structural units but show typical dislocation stress fields. In other words, if we introduce a small twist angle ϕ on a HASTGB ($\theta = \theta_1$) or a small tilt angle θ on a HATwGB ($\phi = \phi_1$), then for the corresponding HAMGBs, equation (3) varies to

$$E_{\text{HAMGB}}^{\text{Total}}(\theta_1, \phi) = E(\theta_1, 0) + \phi \left[E_{\text{LATwGB}}^{\text{Core}} - E_{\text{LATwGB}}^{\text{Strain}} \ln(\phi) \right] + \theta_1 \phi \left[E_{\text{Loss}}^{\text{Core}} - E_{\text{Loss}}^{\text{Strain}} \ln(\theta_1 \phi) \right] \quad (5)$$

and

$$E_{\text{HAMGB}}^{\text{Total}}(\theta, \phi_1) = \theta \left[E_{\text{LASTGB}}^{\text{Core}} - E_{\text{LASTGB}}^{\text{Strain}} \ln(\theta) \right] + E(0, \phi_1) + \theta \phi_1 \left[E_{\text{Loss}}^{\text{Core}} - E_{\text{Loss}}^{\text{Strain}} \ln(\theta \phi_1) \right] \quad (6)$$

respectively. Once we merge the terms $\theta E_{\text{LASTGB}}^{\text{Core}} - \theta E_{\text{LASTGB}}^{\text{Strain}} \ln(\theta)$ and $\theta \phi_1 E_{\text{Loss}}^{\text{Core}} - \theta \phi_1 E_{\text{Loss}}^{\text{Strain}} \ln(\theta \phi_1)$ together, a straightforward form of equations (5) and (6) could be written as

$$E_{\text{HAMGB}}^{\text{Total}}(\theta_1, \phi) = E(\theta_1, 0) + \phi \left[E^{\text{Core}} - E^{\text{Strain}} \ln(\phi) \right] \quad (7)$$

and

$$E_{\text{HAMGB}}^{\text{Total}}(\theta, \phi_1) = \theta \left[E^{\text{Core}} - E^{\text{Strain}} \ln(\theta) \right] + E(0, \phi_1) \quad (8)$$

respectively. Where E^{Core} and E^{Strain} are fitting terms in the classical Read-Shockley relationship [46]. Note that there are some kinds of constraints to equations (7) and (8) because the GB energy at a specific temperature is incapable of exceeding a maximum value E_{max} , no matter how the GB macroscopic and microscopic DOFs change. E_{max} undoubtedly denotes the maximum lattice distortion in the 5D GB space and it can be considered as the maximum degree of lattice disorder of an interface.

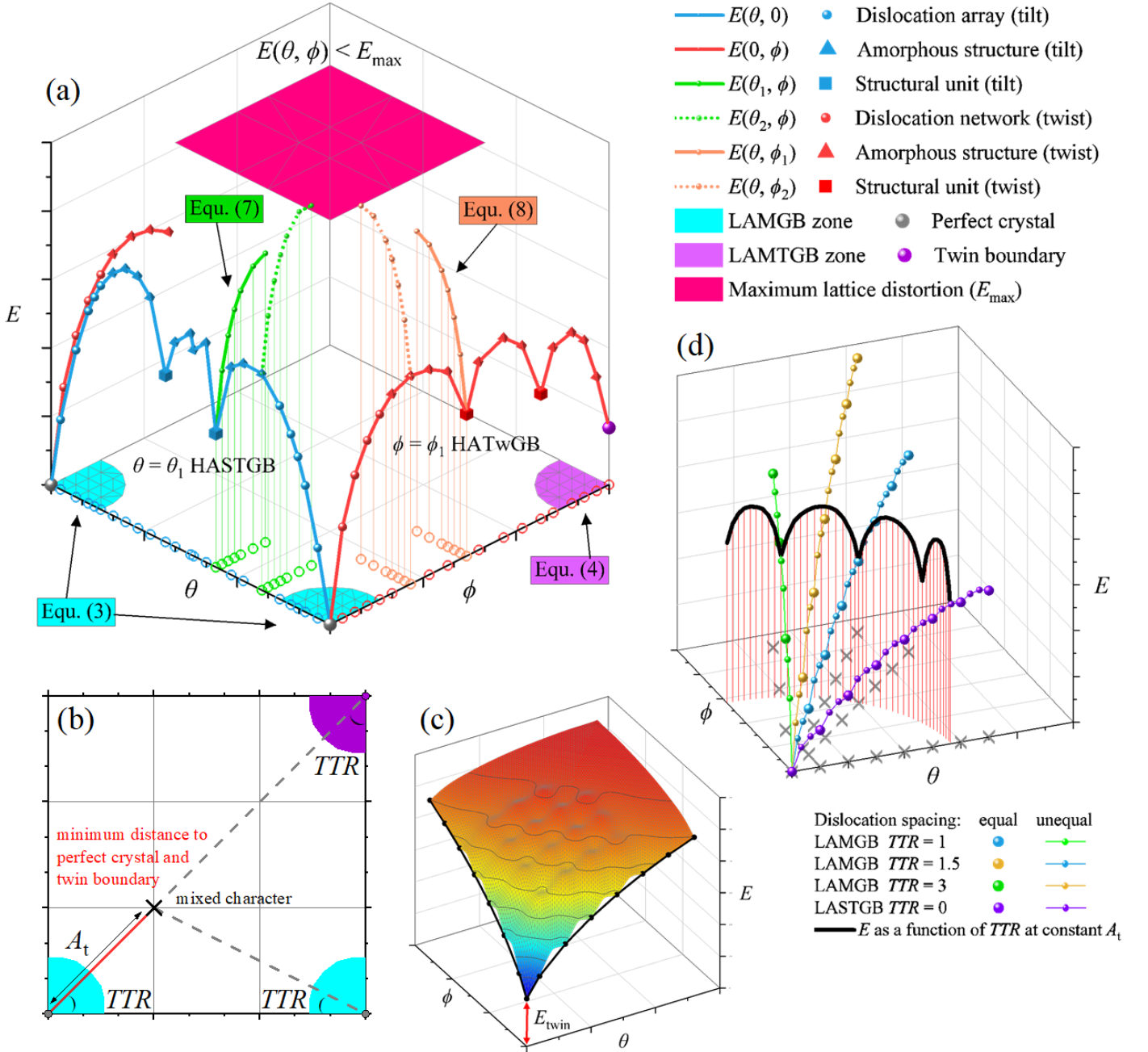


Figure 10. Conceptualization and illustration of the universal Read-Shockley GB energy model in the mixed character space. (a) Assumed energy trend in an assumed mixed character space; (b) Definition of the total misorientation angle A_t in the mixed character space. The following are benefits of using A_t to index mixed GBs: 1) It reflects the role of the parameter TTR in the LAMGB and LAMTGB zones; 2) All dislocation structured GBs are indexed as LAGB; (c) Assumed 2D energy surface near the twin GB. The energy surface is uneven and shows fine cusps because of the unequal dislocation spaces and excess dislocations, as stated in Figure 10d; (d) Assumed GB energy trends in the LAMGB zones as a 2D extension of the 1D Read-Shockley results [46]. Read and Shockley indicated that there will be peaks between two LASTGBs where dislocations are perfectly arranged due to the unequal dislocation spacing. However, parameter TTR contributes to the peaks in the LAMGB zone when LAMGB are not perfectly mixed (excess dislocations if certain TTR value is not satisfied), and such contribution is significantly higher than the contribution of unequal dislocation spacing of LASTGBs and other 1D LAMGB. Note that all data used in Figure 10 is assumed for the illustration and is not reproducible in simulation and experiments.

Equations (2) to (8) and the relevant discussions are summarized in Figure 10a as a universal Read-Shockley model for GB energies in the mixed character space. The applicable range and the functional form of the equations are clearly presented. Figure 10b shows the definition of the total misorientation angle A_t in

the mixed character space. Unlike the conventional definition of misorientation angles in the Rodriguez-Frank space that is frequently used in the literature, A_t of a mixed GB character in a specific mixed character space is defined as its minimum distances (unit: angle) to the positions of all perfect crystals and twin GBs in this space following:

$$A_t = \sqrt{\theta_{\min}^2 + \phi_{\min}^2} \quad (9)$$

Where θ_{\min} and ϕ_{\min} are defined as the minimum tilt and twist angular distances to the positions of all perfect crystals and twin GBs in each mixed character space, respectively. A definition like that allows us to adapt the fact that the dislocation network topology of both LAMGBs and LAMTGBs is governed by the parameter TTR . Also, it guarantees that all dislocation-structured GBs have low A_t values and are considered as LAGBs (LAMTGBs are located near 60° [111] twin GB, and thus they are not considered as LAGBs while using the description of the Rodriguez-Frank space).

Figure 10c shows an assumed high-resolution ($1^\circ \times 1^\circ$) energy surface near the twin GB. To highlight the inherent physical characteristics in the LAMGB and LAMTGB zones, the assumed energy surface is not plotted using real data. The energy surface is not smooth, on the contrary, they are full of deep cusps and high peaks. Equation (4) is only valid for the deep cusps where the dislocations are assumed with equal spacing, while the high peaks are formed by the unequal spacing of the dislocations and the parameter TTR plays an important role here in generating the high peaks. To make the explanation impressive, the authors plotted some assumed energy trends along several specific trace lines in an assumed LAMGB zone shown in Figure 10d. LAMGBs in an arbitrary trace line through the perfect crystal ($\theta = 0^\circ$, $\phi = 0^\circ$) will share the same dislocation network topology, but only a few LAMGBs in this trace line have equal dislocation spacing. Unequal dislocation spacing and/or additional dislocations appear in other LAMGBs, as highlighted by Read and Shockley [46] and double confirmed by Figure 4g1. The energy is peak-like between two LAMGBs characters that have equal dislocation spacing. However, the situation becomes complicated and unexpected for the mixed character space with two co-existing DOFs. It is beyond the expectation of Read and Shockley that the parameter TTR plays an important role in determining both the structures and energies of LAMGBs. Take the chemical reaction for an example, we get one mole of water when two moles of hydrogen and oxygen are fully reacted. However, there will be one mole of water and one mole of oxygen if two moles of hydrogen react with three moles of oxygen. The dislocation structures of LASTGB and LATwGB follow the same rule to form LAMGB. So, once its tilt and twist components are not following certain ratios (e.g., $TTR = 1.5$ LAMGB) there will be excess dislocations (or stacking faults) in a LAMGB that cause significant energy increase. Such a process is illustrated in the black energy line with the same A_t value in Figure 10d. It should be noted that the contribution of the excess dislocations from the parameter TTR to the GB energy is always greater than the contribution of the unequal dislocation spacing. In other words, GB energy suffers lower peaks in the trace line through the perfect crystal, but it suffers higher peaks in the tangent direction of that trace line.

3.3.2. Performance & Transferability

Next, we consider the performance and transferability of the universal Read-Shockley model. The model performance is examined on the general characteristics of the studied mixed GBs. The starting point is to

convert the mixed GB characters to the well-recognized one-dimensional simplified description that is indexed by a single angular scalar, although such simplification ignores the classification of possible GB characters. The authors do not intend to use the conventional description of the misorientation angle in the Rodriguez-Frank space because the role of the twin GB is similar to the perfect crystal in accommodating LAMTGBs. On the contrary, the conception of the total misorientation angle introduced in equation (9) is adapted to convert the three energy surfaces in Figure 2 to the one-dimensional simplification in Figure 11a.

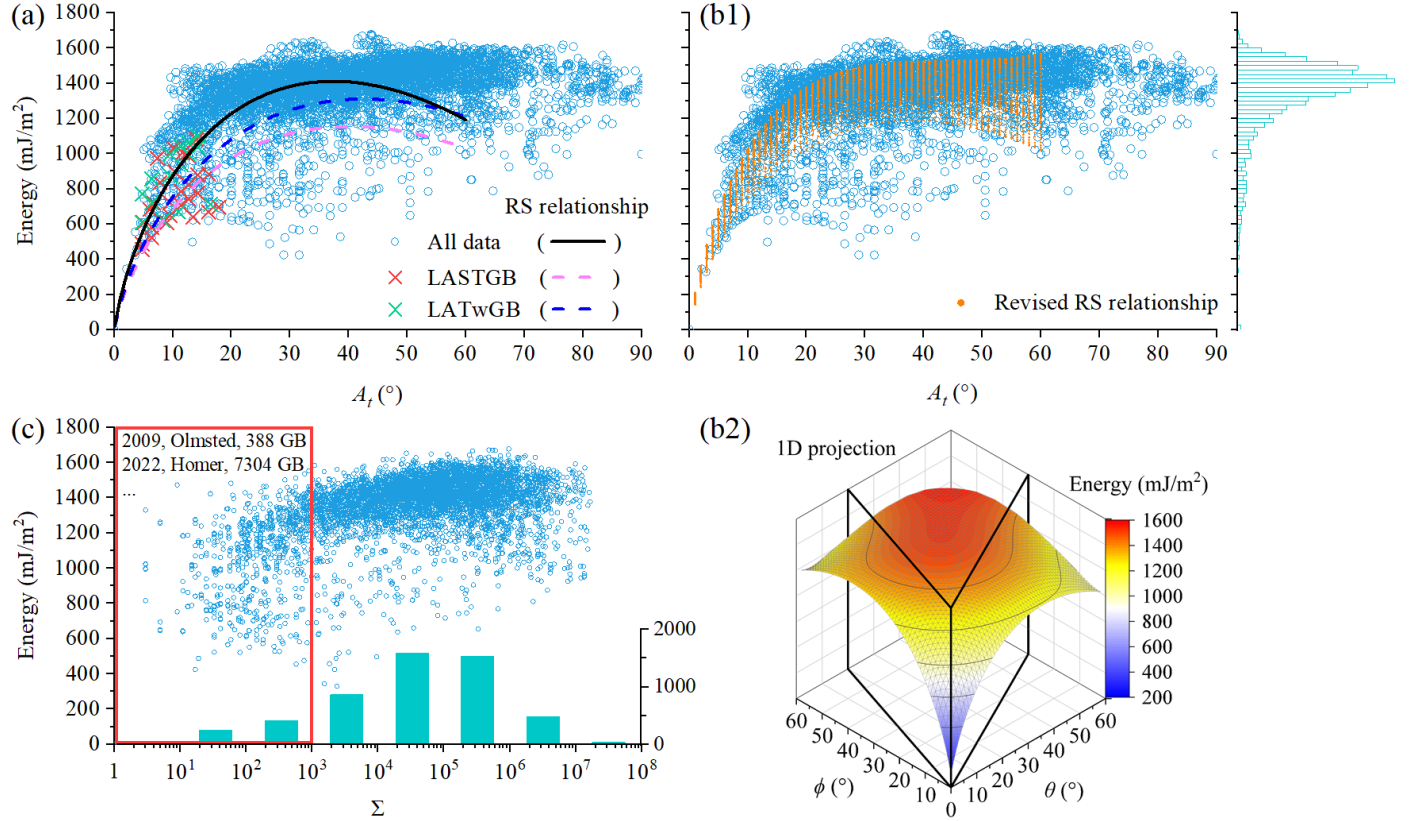


Figure 11. Silicon GB energy against the selected scalars. (a) Silicon GB energy against the total misorientation angle A_t , and the fitting from the Read-Shockley (RS) relationship. All fittings only used data within 60°. (b1) Fitting of the mixed GB energy from the revised Read-Shockley relationship, which is plotted by projecting the two-dimensional energy surface of (b2) to one-dimension. (b2) Two-dimensional energy surface of the data fitting from the revised Read-Shockley relationship. (c) Silicon GB energy against Σ . It indicates that GB energy is gradually approaching a constant value when Σ is higher than 10³.

Figure 11a shows silicon GB energy as a function of A_t , accompanied by the marks of the LAGBs and the three fittings (fitting of all GB energies, LASTGB and LATwGB energies, and fitting data below 60° is shown while the fitting parameters are given in Table 1) from the classical Read-Shockley relationship. It can be seen that the general trends of the mixed GB energy follow the classical Read-Shockley relationship, which is slightly higher than the Read-Shockley fittings of both LASTGB and LATwGB. Figure 11b1 shows the fitting of all GB energies from the revised Read-Shockley relationship, which is plotted by converting the fitted 2D energy surface in Figure 11b2 via the simplification that was previously introduced. Compared with the classical Read-Shockley relationship that connects GB energy with A_t , the revised Read-Shockley relationship shows natural superiority to fit so massive data as its one-dimensional simplification is a cloud-like distribution showing the range of GB energy at any misorientation angles. However, such simplification also suffers two obvious shortages: 1) The value of A_t may be higher than the constrain of the Rodriguez-

Frank space as the mixed GB characters are simplified individually in each energy surface; 2) A given GB character is being indexed multiple times in different energy surfaces and thus unable to ensure the uniqueness of index.

Figure 11c shows silicon GB energy as a function of Σ , from which the common features of the examined mixed GBs could be extracted. The average Σ value is approximately 4.4×10^5 , and most of the mixed GBs have Σ values higher than 10^3 , both of which mean the fruitfulness of GB atomic environments presented here. They note that the energies of most of these high Σ HAMGBs (except for the low energy LAMGBs and LAMTGBs as both can be expressed with high Σ) are approaching a constant value at around 1400 mJ/m^2 . A qualitative explanation is that these high Σ GBs are mostly amorphous structures without any structural units and dislocation structures that may contribute to low energy. The authors are optimistic about the potential of these data as they will provide unique and sufficient samples for machine-learning approaches to advance GB structure-property relationships.

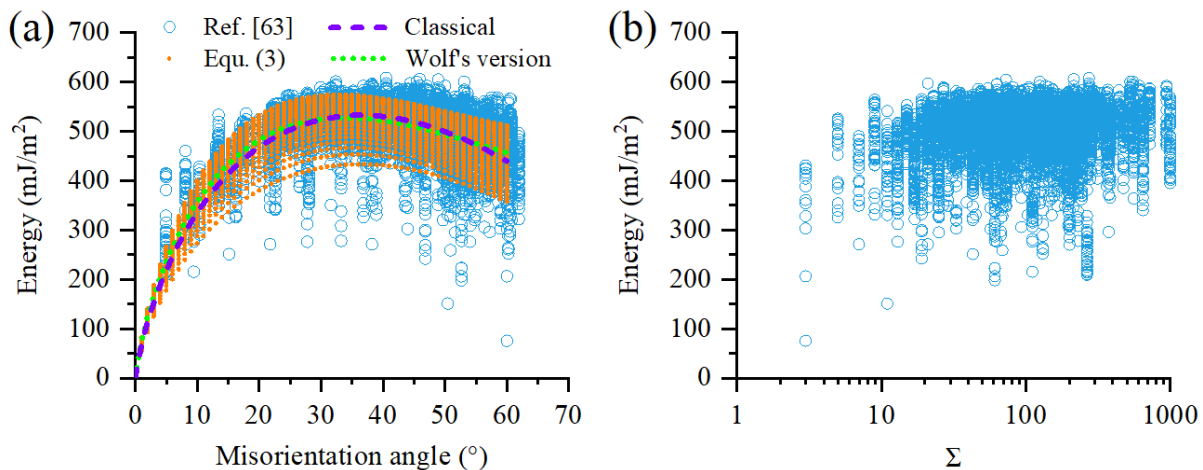


Figure 12. (a) 7304 aluminum GB energies from reference [63] versus the misorientation angle (Rodriguez-Frank space definition). The purple dash line denotes fitting of the classical Read-Shockley relationship [46], and the green dash line denotes fitting of Wolf's version of the Read-Shockley relationship [92]; (b) 7304 aluminum GB energies versus Σ . Noting that authorization for the reuse of these published data has been obtained.

Figure 12 shows the fitting of the revised Read-Shockley relationship on a recently published GB dataset [63] that contains 7304 unique aluminum GBs. The fitting effect of the revised Read-Shockley relationship on aluminum GB is even better than the counterpart on silicon as such a relationship almost perfectly captures the general trend of aluminum GB energy compared with its original functional. The fitting parameters of both silicon and aluminum GBs are given in the Supporting Information, which is expected to be useful in any engineering and scientific application that involves the calculation of the related GB energies. The success of the revised Read-Shockley relationship in predicting both silicon and aluminum GB energy trends could also be extended to a wide range of materials across the FCC and diamond lattice through a key fact that GB energy is scaling with the elastic modulus in those materials with the same lattice [97].

4. Conclusions

The energies and structures of 4964 silicon GBs with mixed tilt and twist characters, as well as their decomposed tilt and twist GB components are studied in this work to confirm whether the mixed GBs follow

the principles of superposition. There are several conclusions worth noting:

- Structures and stress fields of a given mixed GB follow the principles of superposition if it contains a low angle tilt or twist component: 1) LAMGB comprised of dislocation structures (and stacking fault) is the superposition of its tilt and twist components after subjecting energetically favorable dislocation reaction and glide; 2) LAMTGB comprised of dislocation-twin structures and some HAMGBs comprised of completely amorphous structures are also the superposition of their tilt and twist components because we have proved the possibility to introduce dislocation or analogous dislocation structures in structural unit GBs. Qualitatively speaking, the principles of superposition are inversely correlated with both tilt and twist angles.
- A universal Read-Shockley model is proposed from a recently revised Read-Shockley relationship of Wan and Tang [66] on the basis of these reported structural features. This model accurately captures the energy trends of LAMGB and LAMTGB, and shows inherent superiority compared with the classical Read-Shockley relationship. Its universality is extracted by extending to HAMGBs with low angle components, while its transferability is proven by precisely fitting the energy trend of 7304 FCC aluminum GBs. As the supplementary of both the Read-Shockley relationship and this model, we also highlighted the role of parameter TTR because the structures and energies of LAMGB and LAMTGB are especially sensitive to it.
- The simulated GB structures and the derived conclusions are validated in the comparisons between experimental observations and first-principles calculation. Formation mechanisms of mostly LAMGBs are confirmed as the dislocation reaction and glide we reported. First-principles calculation on the energies of low Σ GBs is in good scaling with the atomistic simulation, which not only connects both simulation methods but further reinforces the reliability of the presented energy surface. Notably, our work reports a sub-angstrom level error in atom positions while comparing the simulation and an experimentally investigated HASTGB, and thus makes the presented massive silicon GB structural datasets convincing.

Beyond these conclusions, more intriguing features could be explored further. Our work only addressed the basic structural and energetic features of mixed GBs. It is uncertain whether the other GB properties (e.g., mobility, strength and thermal conductivity) follow the same formalism or justly simply non-linear. Meanwhile, our dataset could also be useful for machine-learning characterization of GB structure-property relationships.

It should also be noted that this work does not address (1) mixed asymmetric tilt and twist GBs; (2) the relative rotation angle between tilt and twist angles. For (1), the authors believe they may follow the same formalism with those studied here. Alternatively, one may use the knowledge of asymmetric tilt GBs to extrapolate. For (2), our previous work has demonstrated that the rotation angle has a close linear impact on the LAMGB structures, but it is still uncertain whether such a close linear impact could be maintained for high angle mixed GBs. To fully understand the GB structure-property correlation across five macroscopic DOFs, more efforts are desired.

Data availability

Numerical data are available upon reasonable request.

Acknowledgements

W. Wan acknowledges the insightful discussions with Prof. E.R. Homer from Brigham Young University. W. Wan also acknowledges the insightful discussions with Prof. J.B. Yang from the Institute of Metal Research, Chinese Academy of Science. W. Wan and C.X. Tang thank Prof. W.N. Zou from Nanchang University for his support.

Competing interests

The authors declare no competing interests.

Fundings

This work was jointly funded by the National Natural Science Foundation of China (grant number: 11802112) and the Institute for Advanced Study of Nanchang University

Author contributions

- 1) W. Wan carried out this project, provided the minor funding, performed all simulations, visualized all figures, theorized the universal Read-Shockley model, wrote the original manuscript and critically revised it.
- 2) C.X. Tang supervised the project, contributed computation resources, maintained the data, provided the major funding, and revised the manuscript with W. Wan.

References

- [1] Rubio, R.A.; Haouala, S.; Llorca, J. Grain boundary strengthening of FCC polycrystals. *J. Mater. Res.* **2019**, *34*, 2263–2274.
- [2] Zhou, Q.; Huang, P.; Liu, M.B.; Wang, F.; Xu, K.W.; Lu, T.J. Grain and interface boundaries governed strengthening mechanisms in metallic multilayers. *J. Alloy. Compd.* **2017**, *698*, 906–912.
- [3] Keast, V.J.; Williams, D.B. Grain boundary chemistry. *Curr. Opin. ST. M.* **2001**, *5*, 23–30.
- [4] Yang, J.B.; Yang, Z.G.; Nagai, Y.; Hasegawa, M. A crystallographic model of FCC/BCC martensitic nucleation and growth. *Acta Mater.* **2010**, *58*, 1599–1606.
- [5] Lehockey, E.M.; Limoges, D.; Palumbo, G.; Sklarchuk, J.; Tomantschger, K.; Vincze, A. On improving the corrosion and growth resistance of positive Pbacid battery grids by grain boundary engineering. *J. Power Sources* **1999**, *78*(1), 79–83.
- [6] Ayuela, A.; Jaskolski, W.; Chico, L. Electronic properties of graphene grain boundaries. *New J. Phys.* **2014**, *16*, 083018.
- [7] Randle, V. Grain boundary engineering: an overview after 25 years. *Mater. Sci. Technol.* **2010**, *26*(3), 253–261.
- [8] Watanabe, T. Grain boundary engineering: historical perspective and future prospects. *J. Mater. Sci.* **2011**, *46*(12), 4095–4115.
- [9] Song, L. H.; Yu, X. G. Defect engineering in cast mono-like silicon: A review. *Prog. Photovoltaics* **2021**, *29*(3), 294–314.
- [10] Kutsukake, K.; Usami, N.; Ohno, Y.; Tokumoto, Y.; Yonenaga, I. Mono-like silicon growth using functional grain boundaries to limit area of multicrystalline grains. *IEEE J. Photovolt.* **2014**, *4*, 1.

- [11] Rittner, J.; Seidman, D. <110> Symmetric tilt grain-boundary structures in fcc metals with low stacking-fault energies. *Phys. Rev. B* **1996**, 54(10), 6999.
- [12] Holm, E.A.; Rohrer, G.S.; Foiles, S.M.; Rollett, A.D.; Miller, H.M.; Olmsted, D.L. Validating computed grain boundary energies in fcc metals using the grain boundary character distribution. *Acta Mater.* **2011**, 59(13), 5250–5256.
- [13] Tschopp M.A.; Coleman, S.P.; McDowell, D.L.; Symmetric and asymmetric tilt grain boundary structure and energy in Cu and Al (and transferability to other fcc metals), *Integr. Mater. Manuf. Innov.* **2015**, 4(1), 176–189.
- [14] Olmsted, D.L. Foiles, S.M., Holm, E.A. Survey of computed grain boundary properties in face-centered cubic metals: I. Grain boundary energy. *Acta Mater.* **2009**, 57, 3694.
- [15] Olmsted, D.L.; Holm, E.A.; Foiles, S.M. Survey of computed grain boundary properties in face-centered cubic metals-II: Grain boundary mobility. *Acta Mater.* **2009**, 57, 3704.
- [16] Homer, E.R. High-throughput simulations for insight into grain boundary structure-property relationships and other complex microstructural phenomena. *Comput. Mater. Sci.* **2019**, 161, 244–254.
- [17] Bair, J.L.; Homer, ER. Antithermal Mobility in $\Sigma 7$ and $\Sigma 9$ Grain Boundaries Caused by Stick-Slip Stagnation of Ordered Atomic Motions about Coincidence Site Lattice Atoms. *Acta Mater.* **2019**, 162, 10–18.
- [18] Priedeman, J.L.; Olmsted, D.L.; Homer, E.R. The role of crystallography and the mechanisms associated with migration of incoherent twin grain boundaries. *Acta Mater.* **2017**, 131, 553–563.
- [19] Homer, E.R. Investigating the mechanisms of grain boundary migration during recrystallization using molecular dynamics. In: 36th Risø International Symposium on Materials Science. Roskilde: IOP Publishing, **2015**, pp.012006.
- [20] Homer, E.R.; Holm, E.A.; Foiles, S.M.; Olmsted, D.L. Trends in Grain Boundary Mobility: Survey of Motion Mechanisms. *JOM* **2014**, 66(1), 114–120.
- [21] Huang, Q.S.; Yang, W.; Zhou, H.F. Migration of grain boundary triple junctions in nanocrystalline metals initiated by accumulated dislocations. *Int. J. Plasticity* **2024**, 173, 103872.
- [22] Page, D.E.; Varela, K.F.; Johnson, O.K.; Fullwood, D.T.; Homer, E.R. Measuring simulated hydrogen diffusion in symmetric tilt nickel grain boundaries and examining the relevance of the Borisov relationship for individual boundary diffusion. *Acta Mater.* **2021**, 212, 116882.
- [23] Wagih, M.; Schuh, C.A. Viewpoint: Can symmetric tilt grain boundaries represent polycrystals? *Scr. Mater.* **2023**, 237, 115716.
- [24] Wagih, M.; Schuh, C.A. Learning Grain-Boundary Segregation: From First Principles to Polycrystals. *Phys. Rev. Lett.* **2022**, 129, 046102.
- [25] Jiang, H.; Szlufarska, I. Small-angle twist grain boundaries as sinks for point defects. *Sci. Rep.* **2018**, 8, 3736.
- [26] Jiang, H.; Wang, X.; Szlufarska, I. The multiple roles of small angle tilt grain boundaries in annihilating radiation damage in SiC. *Sci. Rep.* **2017**, 7, 42358.
- [27] Zhu, Q.; Samanta, A.; Li, B.; Rudd, R.E.; Frolov, T. Predicting phase behavior of grain boundaries with evolutionary search and machine learning. *Nat. Commun.* **2018**, 9(1), 467.
- [28] Han, J.; Vitek, V.; Srolovitz, D.J. Grain-boundary metastability and its statistical properties. *Acta Mater.* **2016**, 104, 259–273.
- [29] Meiners, T.; Frolov, T.; Rudd, R.E.; Dehm, G.; Liebscher, C.H. Observations of grain-boundary phase transformations in an elemental metal. *Nature* **2020**, 579(7799), 375–378.
- [30] Zhang, J.; Wang, C.; Ho, K. Finding the low-energy structures of Si[001] symmetric tilted grain boundaries with a genetic algorithm. *Phys. Rev. B* **2009**, 80, 174102.
- [31] Yu, Z.Y.; Cantwell, P.R.; Gao, Q.; Yin, D.; Zhang, Y.Y.; Zhou, N.X.; Rohrer, G.S.; Widom, M.; Luo, J.; Harmer, M.P. Segregation-induced ordered superstructures at general grain boundaries in a nickel-bismuth alloy. *Science* **2017**, 358, 97–101.
- [32] Von Alffhan, S.; Haynes, P.D.; Kaski, K.; Sutton, A.P. Are the structures of twist grain boundaries in silicon ordered at 0K. *Phys. Rev. Lett.* **2006**, 96, 055505.
- [33] Shiihara, Y.; Kanazawa, R.; Matsunaka, D.; Lobzenko, I.; Tsuru, T.; Kohyama, M.; Mori, H. Artificial neural network molecular mechanics of iron grain boundaries. *Scr. Mater.* **2021**, 207, 114268.

- [34] Yokoi, T.; Kato, H.; Oshima, Y.; Matsunaga, K. Atomic structures of grain boundaries for Si and Ge: A simulated annealing method with artificial-neural-network interatomic potentials. *J. Phys. Chem. Solids* **2022**, *173*, 111114.
- [35] Yokoi, T.; Matsuura, M.; Oshima, Y.; Matsunaga, K. Grain-boundary thermodynamics with artificial-neural-network potential: Its ability to predict the atomic structures, energetics, and lattice vibrational properties for Al. *Phys. Rev. Mater.* **2023**, *7*(5), 053803.
- [36] Gomberg, J.A.; Medford, A.J.; Kalidindi, S.R. Extracting knowledge from molecular mechanics simulations of grain boundaries using machine learning. *Acta Mater.* **2017**, *133*, 100–108.
- [37] Rosenbrock, C.W.; Homer, E.R.; Csányi, G.; Hart, G.L.W. Discovering the building blocks of atomic systems using machine learning: application to grain boundaries. *npj Comput. Mater.* **2017**, *3*(1), 29.
- [38] Sharp, T.A.; Thomas, S.L.; Cubuk, E.D.; Schoenholz, S.S.; Srolovitz, D.J.; Liu, A.J. Machine learning determination of atomic dynamics at grain boundaries. *Proc. Natl. Acad. Sci.* **2018**, *115*(43), 10943–10947.
- [39] Priedeman, J.L.; Rosenbrock, C.W.; Johnson, O.K.; Homer, E.R. Quantifying and connecting atomic and crystallographic grain boundary structure using local environment representation and dimensionality reduction techniques. *Acta Mater.* **2018**, *161*, 431–443.
- [40] Homer, E.R.; Hensley, D.M.; Rosenbrock, C.W.; Nguyen, A.H.; Hart, G.L.W. Machine-learning informed representations for grain boundary structures. *Front. Mater.* **2019**, *6*, 168.
- [41] Patala, S. Understanding grain boundaries - the role of crystallography, structural descriptors and machine learning, *Comput. Mater. Sci.* **2019**, *162*, 281–294.
- [42] Otsuki, A. Energies of (001) twist grain boundaries in silicon. *Acta Mater.* **2001**, *49*, 1737–1745.
- [43] Wang, L.; Yu, W.S.; Shen, S.P. Revisiting the structures and energies of silicon <110> symmetric tilt grain boundaries. *J. Mater. Res.* **2019**, *34*(6), 1021–1033.
- [44] Von Althaus, S.; Kaski, K.; Sutton, A.P. Order and structural units in simulations of twist grain boundaries in silicon at absolute zero. *Phys. Rev. B* **2006**, *74*, 134101.
- [45] Baruffi, C.; Brandl, C. On the structure of (111) twist grain boundaries in diamond: atomistic simulations with Tersoff-type interatomic potentials. *Acta Mater.* **2021**, *215*, 117055.
- [46] Read, W.T.; Shockley, W. Dislocation models of crystal grain boundaries. *Phys. Rev.* **1950**, *78*(3), 275–289.
- [47] Frank, F.C. Conference on plastic deformation of crystalline solids. Carnegie Institute of Technology and Office of Naval Research. **1950**, 150.
- [48] Bilby, B.A. Continuous distribution of dislocations. *Prog. Solid. Mech.* **1960**, *1*, 329.
- [49] Yang, J.B.; Nagai, Y.; Hasegawa, M. Use of the Frank–Bilby equation for calculating misfit dislocation arrays in interfaces. *Scr. Mater.* **2010**, *62*(7), 458–461.
- [50] Yang, J.B.; Nagai, Y.; Yang, Z.G.; Hasegawa, M. Quantization of the Frank–Bilby equation for misfit dislocation arrays in interfaces. *Acta Mater.* **2009**, *57*, 4874–4881.
- [51] Sangghaleh, A.; Demkowicz, M.J. AIDA: a tool for exhaustive enumeration of solutions to the quantized Frank-Bilby equation. *Comput. Mater. Sci.* **2018**, *145*, 35–47.
- [52] Sutton, A.P. On the structural unit model of grain boundary structure. *Philos. Mag. Lett.* **1989**, *59*(2), 53–59.
- [53] Han, J.; Vitek, V.; Srolovitz, D.J. The grain-boundary structural unit model redux. *Acta Mater.* **2017**, *133*, 186–199.
- [54] Banadaki, A.D.; Patala, S. A three-dimensional polyhedral unit model for grain boundary structure in fcc metals. *npj Comput. Mater.* **2017**, *3*(1), 13.
- [55] Winter, I.S.; Rudd, R.E.; Ooppelstrup, T.; Frolov, T. Nucleation of Grain Boundary Phases. *Phys. Rev. Lett.* **2022**, *128*, 035701.
- [56] Winter, I.S.; Ooppelstrup, T.; Frolov, T.; Rudd, R.E. Characterization and visualization of grain boundary disconnections. *Acta Mater.* **2022**, *237*, 118067.
- [57] Saylor, D.M.; Morawiec, A.; Rohrer, G.S. The relative free energies of grain boundaries in magnesia as a function of five macroscopic parameters. *Acta Mater.* **2003**, *51*(13), 3675–3686.
- [58] Brink, T.; Langenohl, L.; Bishara, H.; Dehm, G. Universality of grain boundary phases in fcc metals: Case study on high-angle [111] symmetric tilt grain boundaries. *Phys. Rev. B* **2023**, *107*(5), 054103.

- [59] Homer, E.R.; Patala, S.; Priedeman, J.L. Grain boundary plane orientation fundamental zones and structure-property relationships. *Sci. Rep.* **2015**, *5*, 15476.
- [60] Erickson, H.C.; Homer, E.R. Insights into grain boundary energy structure-property relationships by examining computed [1 0 0] disorientation axis grain boundaries in Nickel. *Scr. Mater.* **2020**, *185*, 165–169.
- [61] Patala, S.; Schuh, C.A. Symmetries in the representation of grain boundary plane distributions. *Philos. Mag.* **2013**, *93*(5), 524–573.
- [62] Baird, S.G.; Homer, E.R.; Fullwood, D.T.; Johnson, O.K. Five degree-of-freedom property interpolation of arbitrary grain boundaries via Voronoi fundamental zone framework. *Comput. Mater. Sci.* **2021**, *200*, 110756.
- [63] Homer, E.R.; Hart, G.L.W.; Owens, C.B.; Hensley, D.M.; Spendlove, J.C.; Serafinb, L.H. Examination of computed aluminium grain boundary structures and energies that span the 5D space of crystallographic character. *Acta Mater.* **2022**, *234*, 118006.
- [64] Morawiec, A.; Glowinski, K. On “macroscopic” characterization of mixed grain boundaries. *Acta Mater.* **2013**, *61*, 5756–5767.
- [65] Morawiec, A. On the frequency of occurrence of tilt and twist grain boundaries. *Scr. Mater.* **2009**, *61*(4), 438–440.
- [66] Wan, W.; Tang, C.X. Structures and energies of computed silicon (001) small angle mixed grain boundaries as a function of three macroscopic characters. *Acta Mater.* **2023**, *261*, 119353.
- [67] Yang, J.B.; Nagai, Y.; Hasegawa M.; Osetsky, Y.N. Atomic scale modeling of {110} twist grain boundaries in α -iron: structure and energy properties. *Philos. Mag.* **2010**, *90*, 991–1000.
- [68] Yang, J.B.; Osetsky, Y.N.; Stoller, R.E.; Nagai, Y.; Hasegawa, M. The effect of twist angle on anisotropic mobility of {110} hexagonal dislocation networks in α -iron. *Scr Mater.* **2012**, *66*, 761–764.
- [69] Wan, W.; Tang, C.X.; Zou, W.N. Exploring Silicon [001] Small Angle Symmetric Tilt Grain Boundaries: Structures, Energies and Stress fields. *Applied Surface Science* **2022**, *599*, 153828.
- [70] Tang, C.X.; Wan, W.; Huang, L.F.; He, R.C.; Zhou, L. On the Formation and Multiplicity of Si [001] Small Angle Symmetric Tilt Grain Boundaries: Atomistic Simulation of Directional Growth. *Cryst. Growth Des.* **2022**, *22*, 7491–7500.
- [71] Wan, W.; Sun, Z.P.; Xiong, Z.K. Tang, C.X. Misorientation and Temperature Dependence of Small Angle Twist Grain Boundaries in Silicon: Atomistic Simulation of Directional Growth. *Cryst. Growth Des.* **2023**, *23*, 2893–2904.
- [72] Neily, S.; Youssef, S.; Fournel, F.; Bonnet, R. The angular dislocation parallel to a free surface: Application to a (111)Si low-angle twist boundary. *Philos. Mag.* **2011**, *91*(31), 4001–4012.
- [73] Fournel, F.; Moriceau, H.; Aspar, B. Accurate control of the misorientation angles in direct wafer bonding. *Appl. Phys. Lett.* **2002**, *80*, 793.
- [74] Akatsu, T.; Scholz, R.; Gosele, U. Dislocation structure in low-angle interfaces between bonded Si(001) wafers. *J. Mater. Sci.* **2004**, *39*(9), 3031–3039.
- [75] Vdovin, V.I.; Ubyivovk, E.V.; Vyvenko, O.F. Regularities in the Formation of Dislocation Networks on the Boundary of Bonded Si (001) Wafers. *Semiconductors* **2013**, *47*(2), 264–268.
- [76] Vdovin, V.I.; Vyvenko, O.F.; Ubyivovk, E.V.; Kononchuk, O. Mechanisms of Dislocation Network Formation in Si(001) Hydrophilic Bonded Wafers. *Solid State Phenomena* **2011**, *178*, 253.
- [77] Wilhelm, T.; Kuhlmann, V.; Scheerschmidt, K. Bonded semiconductor interfaces with twist and tilt rotation: TEM analysis supported by molecular dynamics structure modelling. *Phys. Stat. Sol. C* **2007**, *4*(8), 3115–3119.
- [78] Lim, A.T.; Haataja, M.; Cai, W.; Srolovitz, D.J. Stress-driven migration of simple low-angle mixed grain boundaries. *Acta Mater.* **2012**, *60*, 1395–1407.
- [79] Thompson, A.P.; Aktulga, H.M.; Berger, R.; Bolintineanu, D.S.; Brown, W.N.; Crozier, P.S.; Veld, P.J.I.; Kohlmeyer, A.; Moore, S.G.; Nguyen, T.D.; Shan, R.; Stevens, M.J.; Tranchida, J.; Trott, C.; Plimpton, S.J. LAMMPS—a flexible simulation tool for particle-based materials modeling at the atomic, meso, and continuum scales. *Comput. Phys. Commun.* **2021**, *271*, 108171.
- [80] Kumagai, T.; Izumi, S.; Hara, S.; Sakai, S. Development of bond-order potentials that can reproduce the elastic constants and melting point of silicon for classical molecular dynamics simulation. *Comput. Mater. Sci.* **2007**, *39*(2), 457–464.

- [81] Kresse, G.; Furthmüller, J. Efficiency of ab-initio total energy calculations for metals and semiconductors using a plane-wave basis set. *Comput. Mater. Sci.* **1996**, *6*, 15–50.
- [82] Kresse, G.; Furthmüller, J. Efficient iterative schemes for ab initio total-energy calculations using a plane-wave basis set. *Phys. Rev. B* **1996**, *54*, 11169.
- [83] Perdew, J.P.; Burke, K.; Ernzerhof, M. Generalized gradient approximation made simple. *Phys. Rev. Lett.* **1996**, *77*, 3865–3868.
- [84] Blöchl, P. E. Projector augmented-wave method. *Phys. Rev. B* **1994**, *50*, 17953.
- [85] Stukowski, A.; Bulatov, V. V.; Arsenlis, A. Automated identification and indexing of dislocations in crystal interfaces. *Model. Simul. Mater. Sc.* **2012**, *20*, 85007.
- [86] Stukowski, A. Visualization and analysis of atomistic simulation data with ovito—the open visualization tool. *Model. Simul. Mater. Sc.* **2010**, *18*, 015012.
- [87] Wan, W.; Tang, C.X.; Zhang, J.J.; Zhou, L. General molecular dynamics approach to understand the mechanical anisotropy of monocrystalline silicon under the nanoscale effects of point defect. *Nanomaterials* **2021**, *11*(8), 1965.
- [88] Bulatov, V.V.; Reed, B.W.; Kumar, M. Grain boundary energy function for fcc metals. *Acta Mater.* **2014**, *65*, 161–175.
- [89] Chirayutthanasak, O.; Sarochawikasit, R.; Khongpia, S.; Okita, T.; Dangtip, S.; Rohrer, G.S.; Ratanaphan, S. Universal function for grain boundary energies in bcc metals. *Scr. Mater.* **2024**, *240*, 115821.
- [90] Ke T.S. A Grain Boundary Model and the Mechanism of Viscous Intercrystalline Slip. *J. Appl. Phys.* **1949**, *20*(3), 274–280.
- [91] Reiche, M.; Kittler, M.; Scholz, R.; Hähnel, A.; Arguirov, T. Structure and properties of dislocations in interfaces of bonded silicon wafers. *Journal of Physics: Conference Series* **2011**, *281*, 012017.
- [92] Bonnet, R.; Couillard, M.; Dhouibi, S.; Neily, S. Atomic scale displacement field induced by a near- $\Sigma 9$ twin boundary in silicon. *Phys. Status Solidi B*, **2016**, 1–4.
- [93] Dai, S.Y.; Xiang, Y.; Srolovitz, D.J. Structure and energy of (1 1 1) low-angle twist boundaries in Al, Cu and Ni. *Acta Mater.* **2013**, *61*, 1327–1337.
- [94] Dai, S.Y.; Xiang, Y.; Srolovitz, D.J. Atomistic, generalized peierls-nabarro and analytical models for (111) twist boundaries in al, cu and ni for all twist angles. *Acta Mater.* **2014**, *69*, 162–174.
- [95] Wolf, D. A Read-Shockley model for high-angle grain boundaries, *Scr. Metall.* **1989**, *23*(10), 1713–1718.
- [96] Schwartz, D.; Bristowe, P.D.; Vitek, V. Dislocation structure and energy of high angle [001] twist boundaries: A computer simulation study. *Acta Metall.* **1988**, *36*(3), 675–687.
- [97] Holm, E.A.; Olmsted, D.L.; Foiles, S.M. Comparing grain boundary energies in face-centered cubic metals: Al, Au, Cu and Ni *Scr. Mater.* **2010**, *63*, 905-908.